NASA/TM-2022-104606/Vol. 61

Technical Report Series on Global Modeling and Data Assimilation, Volume 61

Randal D. Koster, Editor

Validation Assessment for the Soil Moisture Active Passive (SMAP) Level 4 Carbon (L4_C) Data Product Version 6

John S. Kimball, K. Arthur Endsley, Tobias Kundig, Joseph Glassy, Rolf H. Reichle and Joseph V. Ardizzone

April 2022

NASA STI Program ... in Profile

Since its founding, NASA has been dedicated to the advancement of aeronautics and space science. The NASA scientific and technical information (STI) program plays a key part in helping NASA maintain this important role.

The NASA STI program operates under the auspices of the Agency Chief Information Officer. It collects, organizes, provides for archiving, and disseminates NASA's STI. The NASA STI program provides access to the NTRS Registered and its public interface, the NASA Technical Reports Server, thus providing one of the largest collections of aeronautical and space science STI in the world. Results are published in both non-NASA channels and by NASA in the NASA STI Report Series, which includes the following report types:

- TECHNICAL PUBLICATION. Reports of completed research or a major significant phase of research that present the results of NASA Programs and include extensive data or theoretical analysis. Includes compilations of significant scientific and technical data and information deemed to be of continuing reference value. NASA counterpart of peer-reviewed formal professional papers but has less stringent limitations on manuscript length and extent of graphic presentations.

- TECHNICAL MEMORANDUM. Scientific and technical findings that are preliminary or of specialized interest, e.g., quick release reports, working papers, and bibliographies that contain minimal annotation. Does not contain extensive analysis.

- CONTRACTOR REPORT. Scientific and technical findings by NASA-sponsored contractors and grantees.

- CONFERENCE PUBLICATION. Collected papers from scientific and technical conferences, symposia, seminars, or other meetings sponsored or co-sponsored by NASA.

- SPECIAL PUBLICATION. Scientific, technical, or historical information from NASA programs, projects, and missions, often concerned with subjects having substantial public interest.

- TECHNICAL TRANSLATION. English-language translations of foreign scientific and technical material pertinent to NASA's mission.

Specialized services also include organizing and publishing research results, distributing specialized research announcements and feeds, providing information desk and personal search support, and enabling data exchange services.

For more information about the NASA STI program, see the following:

- Access the NASA STI program home page at http://www.sti.nasa.gov

- E-mail your question to help@sti.nasa.gov

- Phone the NASA STI Information Desk at 757-864-9658

- Write to:
  NASA STI Information Desk
  Mail Stop 148
  NASA Langley Research Center
  Hampton, VA 23681-2199

NASA/TM-2022-104606/Vol. 61

Technical Report Series on Global Modeling and Data Assimilation, Volume 61

Randal D. Koster, Editor

Validation Assessment for the Soil Moisture Active Passive (SMAP) Level 4 Carbon (L4_C) Data Product Version 6

John S. Kimball
University of Montana, Missoula, MT

K. Arthur Endsley
University of Montana, Missoula, MT

Tobias Kundig
University of Montana, Missoula, MT

Joseph Glassy
Lupine Logic, Inc., Missoula, MT

Rolf H. Reichle
NASA Goddard Space Flight Center, Greenbelt, MD

Joseph V. Ardizzone
Science Systems and Applications Inc., Lanham, MD

National Aeronautics and
Space Administration

Goddard Space Flight Center
Greenbelt, Maryland 20771

April 2022

Level of Review: This material has been technically reviewed by technical management.

Available from

NASA STI Program
Mail Stop 148
NASA's Langley Research
Center Hampton, VA
23681-2199

National Technical Information
Service 5285 Port Royal Road
Springfield, VA 22161
703-605-6000

TABLE OF CONTENTS

This page intentionally left blank.

EXECUTIVE SUMMARY

The post-launch Cal/Val phase of the Soil Moisture Active Passive (SMAP) satellite mission is guided by two primary objectives for each science product team: 1) to calibrate, verify, and improve the performance of the science algorithms, and 2) to validate the accuracy of the science data products as specified in the SMAP Level-1 mission science requirements. This report provides an assessment of the latest (Version 6) SMAP Level 4 Carbon (L4_C) product. The L4_C Version 6 (v6) global record now spans approximately seven years (March 2015 – present) of SMAP science operations and has benefited from six major reprocessing updates to the operational product. These reprocessing events and L4_C product release updates have incorporated various algorithm refinements and calibration adjustments to account for similar refinements to upstream SMAP brightness temperature retrievals, the GEOS land model assimilation system, and SMAP Level 4 Soil Moisture (L4_SM) inputs used for L4_C processing.

The SMAP L4_C algorithm utilizes a Terrestrial Carbon Flux (TCF) model informed by daily surface and root zone soil moisture information from the SMAP L4_SM product, along with optical remote sensing-based (i.e., from the Moderate Resolution Imaging Spectroradiometer, MODIS, or the Visible Infrared Imaging Radiometer Suite, VIIRS) land cover and canopy fractional photosynthetic active radiation (fPAR), and other ancillary biophysical data. The L4_C product provides estimates of global daily net ecosystem CO_2 exchange (NEE) and the component carbon fluxes, namely, vegetation gross primary production (GPP) and soil heterotrophic respiration (RH). Other L4_C product elements include surface (~0-5 cm depth) soil organic carbon (SOC) stocks and associated environmental constraints to these processes, including soil moisture-related controls on GPP and ecosystem respiration (Kimball et al. 2014, Jones et al. 2017). The L4_C product addresses SMAP carbon cycle science objectives by: 1) providing a direct link between terrestrial carbon fluxes and underlying freeze/thaw and soil moisture-related constraints to these processes, 2) documenting primary connections between terrestrial water, energy and carbon cycles, and 3) improving understanding of terrestrial carbon sink activity.

The SMAP L4_C algorithm and operational product are mature and at a CEOS Validation Stage 4 level (Jackson et al. 2012) based on extensive validation of the multi-year record against a diverse array of independent benchmarks, well-characterized global performance, and systematic refinements gained from six major reprocessing events. There are no Level-1 mission science requirements for the L4_C product; however, self-imposed requirements have been established focusing on NEE as the primary product field for validation, and on demonstrating L4_C accuracy and success in meeting product science requirements (Jackson et al. 2012). The other L4_C product fields also have strong utility for carbon science applications (e.g., Liu et al. 2019, Endsley et al. 2020); however, analysis of these other fields is considered secondary relative to primary validation activities focusing on NEE. The L4_C targeted accuracy requirements are to meet or exceed a mean unbiased root-mean-square (RMS) error (ubRMSE, or standard deviation of the error) for NEE of 1.6 g C m^{-2} d^{-1} or 30 g C m^{-2} yr^{-1}, emphasizing northern (≥45°N) boreal and arctic ecosystems; this accuracy is similar to that of tower eddy covariance measurement-based observations (Baldocchi 2008).

Methods used for the L4_C v6 product performance and validation assessment have been established from the SMAP Cal/Val plan and previous studies (Jackson et al. 2012, Jones et al. 2017; Endsley et al. 2020) and include: 1) consistency evaluations of the product fields against earlier product releases (version 5 or earlier); 2) comparisons of daily carbon flux estimates with independent tower eddy covariance measurement-based daily carbon (CO_2) flux observations from core tower validation sites (CVS); and 3) consistency checks against other global carbon products, including soil carbon inventory records, global GPP records derived from tower observation upscaling methods, and satellite-based observations of canopy solar induced chlorophyll fluorescence (SIF) as a surrogate for GPP. Metrics used to evaluate agreement between L4_C product fields and observational benchmarks include correlation (r-value), RMS differences, bias, and model sensitivity diagnostics. Following these validation criteria, the present report provides a validation assessment of the L4_C v6 product. Detailed descriptions of the L4_C algorithm and additional global product accuracy and performance results are given elsewhere (Jones et al. 2017, Endsley et al. 2020).

The L4_C v6 product replaces earlier product versions and continues to show: (i) accuracy and performance levels meeting or exceeding SMAP L4_C science requirements; (ii) continuing improvements over earlier product versions (v5 and earlier); and (iii) suitability for a diversity of science applications. Example L4_C applications from the recent literature include clarifying environmental trends and controls on the northern terrestrial carbon sink (Liu et al. 2019, Endsley et al. 2022); diagnosing ecosystem productivity behavior in response to extreme climatic events including droughts and heatwaves (Li et al. 2020, Kwon et al. 2021); and regional monitoring of cropland conditions for projecting annual crop yields (Wurster et al. 2020).

1 EXPECTED L4_C ALGORITHM AND PRODUCT PERFORMANCE

The performance of the Soil Moisture Active Passive (SMAP) mission Level 4 Carbon (L4_C) algorithm, including variance and uncertainty estimates of model outputs, was determined during the mission pre-launch phase through spatially explicit model sensitivity studies using available model inputs similar to those currently being used for operational production and evaluating the resulting model simulations over the observed range of northern (≥45 °N) and global conditions (Kimball et al. 2012, Entekhabi et al. 2014). The L4_C algorithm options were also evaluated during the mission prelaunch phase, including deriving canopy fractional photosynthetic active radiation (fPAR) from lower-order satellite NDVI (Normalized Difference Vegetation Index) inputs in lieu of using the Moderate Resolution Imaging Spectroradiometer (MODIS) fPAR (MOD15) product; and including an explicit model representation of boreal fire disturbance recovery impacts. These results indicated that the L4_C accuracy requirements (i.e., NEE[*] ubRMSE[†] ≤ 30 g C m^{-2} yr^{-1} or ≤ 1.6 g C m^{-2} d^{-1}) could be met over more than 82% and 89% of global and northern vegetated land areas, respectively (Yi et al. 2013, Kimball et al. 2014).

The global L4_C algorithm error budget for NEE derived during the mission prelaunch phase indicated that the estimated NEE ubRMSE uncertainty is proportional to GPP and is therefore larger in higher biomass productivity areas, including forests and croplands (Kimball et al. 2014). Likewise, NEE ubRMSE uncertainty is expected to be lower in less-productive areas, including grasslands and shrublands. Expected model NEE ubRMSE levels were also generally within targeted accuracy levels for characteristically less-productive boreal and Arctic biomes, even though relative model error as a proportion of productivity (NEE RMSE / mean GPP) may be large in these areas. The estimated NEE uncertainty was lower than expected in some warmer, tropical, high-biomass productivity areas (e.g. Amazon rainforest) because of reduced temperature and moisture constraints to the L4_C respiration calculations so that the bulk of model uncertainty is contributed by GPP in these areas. Model NEE uncertainty in the African Congo was estimated to be relatively larger than in Amazonia due to relatively drier climate conditions in central Africa and associated larger uncertainty contributions of soil moisture and temperature inputs to the model respiration and GPP calculations.

Detailed global L4_C product assessments and validation activities conducted during the SMAP post-launch Cal/Val and extended mission phases have confirmed that the operational product accuracy and performance is consistent with SMAP L4_C science requirements and product design specifications (e.g., Jones et al. 2017, Endsley et al. 2020, Endsley et al. 2022). The latest v6 product release is expected to show consistent or better performance over earlier product versions (v5 or earlier) versus independent observational benchmarks; the L4_C v6 record is also expected to show no anomalous artifacts or inconsistencies over the extended operational record.

---

[*]Net ecosystem CO_2 exchange.

[†]Unbiased root-mean-square (RMS) error (or standard deviation of the error).

2 PRODUCT (v6) UPDATES FROM PRIOR (v5) RELEASE

The latest SMAP L4_C v6 release includes the following updates from the prior v5 product:

- L4_C processing uses daily soil moisture and temperature inputs from the latest version (v6) of the SMAP operational Level 4 Soil Moisture (L4_SM) product (Reichle et al. 2022). L4_SM v6 processing uses the latest version of the GEOS land modeling system (i.e., Nature Run version NRv9.1 for v6 vs NRv8.3 for v5), which uses precipitation observations from the Integrated Multi-SatellitE Retrievals for GPM (IMERG) product; satellite/gauge IMERG-Final precipitation data is used for L4_SM processing from data day March 31st, 2015 to June 29, 2021 and satellite-only IMERG-Late data thereafter (see also section 3.2).
- We recalibrated the L4_C model Biome Properties Lookup Table (BPLUT) and re-initialized the model surface soil organic carbon (SOC) pools using MODIS Collection 6 fPAR (Myneni et al. 2015), MERRA-2 reanalysis daily surface meteorology (Gelaro et al. 2017), and SMAP L4_SM Nature Run (NRv9.1) daily soil moisture and temperature inputs; the BPLUT recalibration uses tower eddy covariance CO_2 flux records from 329 sites covering all major global plant functional type (PFT) classes represented in the La Thuile and FLUXNET2015 tower synthesis records (Pastorello et al. 2020, Ukkola et al. 2021).
- Model BPLUT soil litter decay rates were adjusted to improve SOC agreement with global soil inventory data, particularly for evergreen broadleaf forest (EBF) areas in the humid tropics.
- The L4_C software used for pre-processing of model inputs was updated to provide a seamless switch between alternative 8-day fPAR inputs provided from either NASA Terra MODIS (MOD15) or from Visible Infrared Imaging Radiometer Suite (VIIRS) (VNP15) operational product streams; MOD15 fPAR remains the baseline for L4_C processing, while the added VNP15 capability enhances L4_C operational resiliency given that the NASA EOS Terra satellite is near the end of its effective mission life.
- All changes were limited to model inputs, pre-processing, and ancillary files, with no changes to the core L4_C algorithm.

3 ASSESSMENTS

3.1 Global v6 differences from prior product release (v5)

General global patterns and seasonal dynamics of the major L4_C land parameters were evaluated in the latest (v6) product to confirm that the model outputs capture characteristic global environmental behavior and show general consistency with the previous (v5) L4_C operational record. These assessments were conducted using the multi-year SMAP record (2015-2020) and also used to identify any potential model errors or anomalies that might require further inspection and more detailed error diagnostics. The L4_C model processing is conducted at a daily time step and 1-km spatial resolution benefitting from MODIS fPAR and land cover (PFT) inputs at this spatial resolution. The L4_C product outputs are posted to a 9-km resolution global EASE-grid (version 2.0; Brodzik et al. 2012), consistent with that of the SMAP L4_SM daily soil moisture and temperature inputs. Primary L4_C product fields include gross primary production (GPP) and soil heterotrophic respiration (RH), which together determine NEE. The L4_C daily product fields also include surface (0-5 cm depth) SOC, derived as the difference between estimated soil litterfall inputs from GPP and respired carbon (CO_2) losses from soil litter decomposition and RH.

3.1.1 Gross Primary Production (GPP)

The mean annual GPP pattern from the latest L4_C v6 (Vv6042) and previous v5 (Vv5040) products is illustrated in **Figure 1** for 2020, one of the warmest years of record globally. The v6 product captures the characteristic global pattern in ecosystem productivity and is largely consistent with the v5 product. GPP generally follows energy and moisture related controls on vegetation growth. Productivity is greatest in wet tropical forest regions, including Amazonia, Congo basin, and Southeast Asia, where nearly optimal conditions for vegetation growth occur throughout the year. GPP is intermediate over croplands and temperate forests, and lower over the high latitudes due to greater seasonality in light, temperature, and moisture related restrictions to productivity. GPP is also lower over semi-arid grasslands and arid deserts due to strong moisture constraints to growth. While the v6 and v5 GPP records are largely consistent, the v6 record indicates slightly less productivity in wet tropical and boreal regions dominated by respective evergreen broadleaf forest (EBF) and deciduous needleleaf forest (DNF) land cover types. The v6 record also shows a small level of productivity enhancement in other regions, including semi-arid and arid regions. Overall, the differences between the v6 and v5 GPP records are small (within ~5%) and reflect minor calibration adjustments to the ancillary BPLUT, particularly for the EBF and DNF PFT classes. The productivity differences also reflect upstream changes to the L4_SM daily soil moisture and soil temperature records used as L4_C model inputs (Reichle et al. 2022). Some of the v6 GPP enhancement in semi-arid regions within the 60N-S degree latitude band reflect soil moisture-related changes in the SMAP v6 L4_SM inputs introduced from using IMERG precipitation in the L4_SM v6 land modeling system (Colliander et al. 2022).

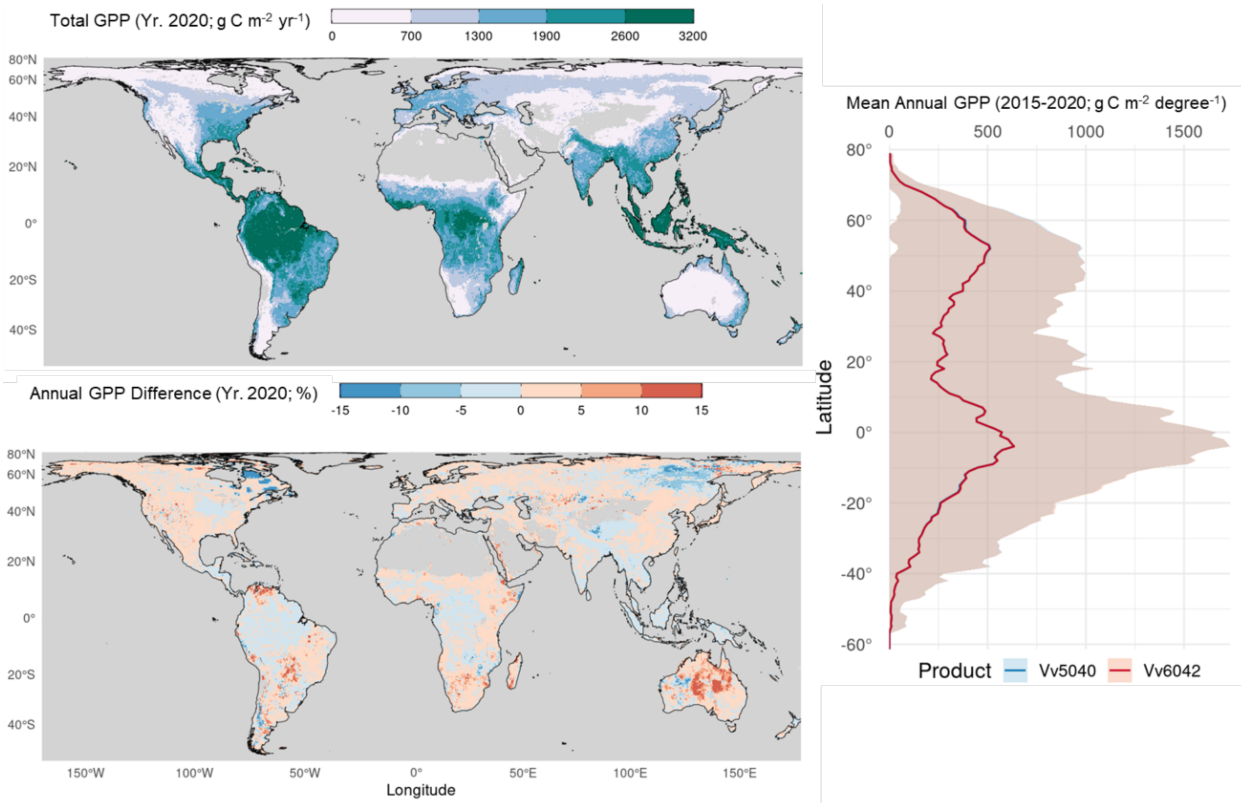

Figure 1. Global pattern of estimated annual GPP for 2020 extracted from the SMAP L4_C v6 data record (top left); the relative difference (%) in annual GPP between the v6 and previous v5 records is also shown (lower left) along with the 1-degree latitude binned spatially averaged GPP for 2015-2020 from each record (right; curves are essentially coincident); shading in the line plot denotes 1 spatial standard deviation within each latitude bin (red and blue shading are essentially coincident). The v6 GPP pattern is largely consistent with the previous v5 record and shows only minor regional differences that reflect updates to the L4_C model inputs and BPLUT recalibration process.

The multi-year (2015-2020) seasonal patterns in estimated GPP from L4_C v6 (Vv6042) and v5 (Vv5040) daily records are shown in **Figure 2** for major land regions defined from the TransCom-3 CO_2 inversion intercomparison (Baker et al. 2006). Both records are strongly overlapping, with minimal differences. The v6 record captures the expected global and seasonal patterns and shows no apparent artifacts or anomalous behavior. The expected patterns represented include an increasing seasonal amplitude in productivity moving from the tropics to the higher latitudes, and general consistency in GPP magnitudes and seasonal cycles spanning the multi-year record in the different regions. Generally higher rates of productivity occur throughout the year over the tropics, but with a marked seasonal cycle that reflects variations in cloud cover and rainfall between wet and dry seasons. The tropical regions also show larger daily variations in GPP due to the greater influence of cloud cover and light availability on fPAR and productivity in the tropics, compared with temperature and soil moisture related controls that have greater impact in other biomes. The larger GPP variability in the tropics also reflects greater data loss and gap-filling of the MODIS fPAR record due to more extensive atmosphere cloud and aerosol contamination in this region relative to other biomes.

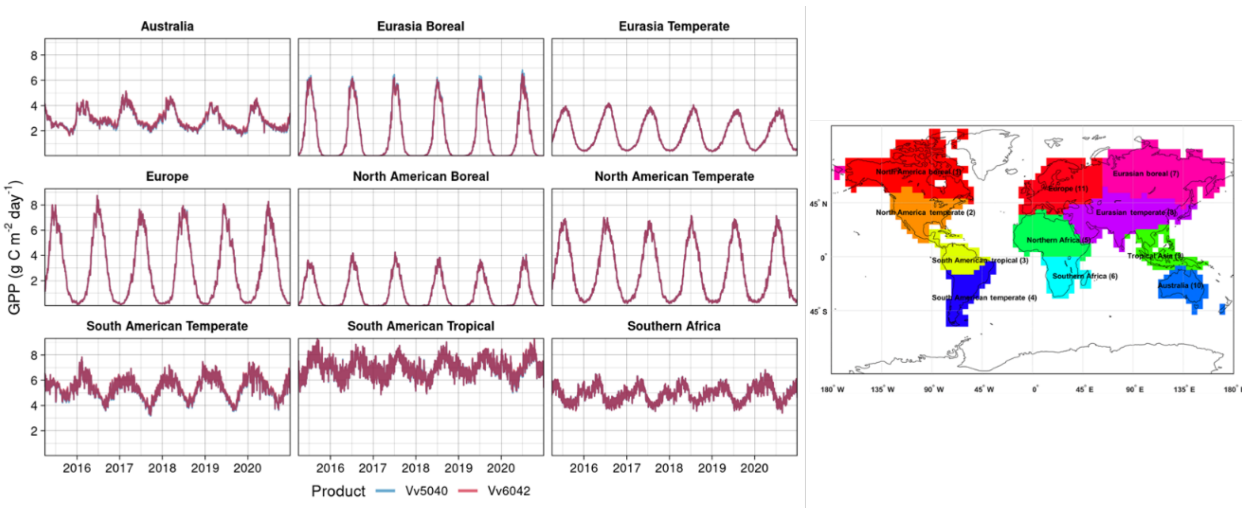

Figure 2. GPP multi-year seasonal patterns derived from L4_C v6 (Vv6042) and v5 (Vv5040) records, averaged within selected major TransCom-3 land regions (right). The latest v6 record is nearly identical to the previous v5 record in representing GPP seasonal cycles and annual variability within these regions.

3.1.2 Heterotrophic Respiration (RH)

The estimated mean annual soil heterotrophic respiration (RH) pattern for 2020 from the L4_C v6 and v5 products is shown in **Figure 3**. The RH pattern is similar to that of GPP owing to the dependence of soil respiration and SOC on litterfall (which is proportional to GPP) and owing to similar soil moisture and temperature-related controls on photosynthesis and respiration. The v6 and v5 records are largely consistent in depicting the characteristic global RH pattern. RH is generally greatest in the wet tropics, where GPP is largest and soil temperature and moisture conditions are optimal for SOC decomposition. RH rates are lowest in sparsely vegetated cold and arid climates due to increasing cold temperature and soil moisture-related constraints on soil decomposition, as well as to relatively low SOC accumulation because of minimal productivity. RH is slightly lower over the tropics in the v6 record relative to v5 owing to the aforementioned reduction in GPP and corresponding reduction in the SOC pool available for soil decomposition in EBF dominant areas. The v6 RH is also lower in DNF dominant areas of northeast Eurasia due to BPLUT recalibration adjustments reducing GPP. Elsewhere, the v6 RH is enhanced compared to the v5 record in many global dryland regions stemming from the influence of IMERG precipitation on the L4_SM soil moisture and temperature inputs used to define the environmental constraints to GPP and soil respiration during L4_C processing. Overall, the difference in RH between the v6 and v5 records is minimal over most of the global domain, except for the tropics, where the records are nonetheless still within 15% of each other, even in the wet tropics.

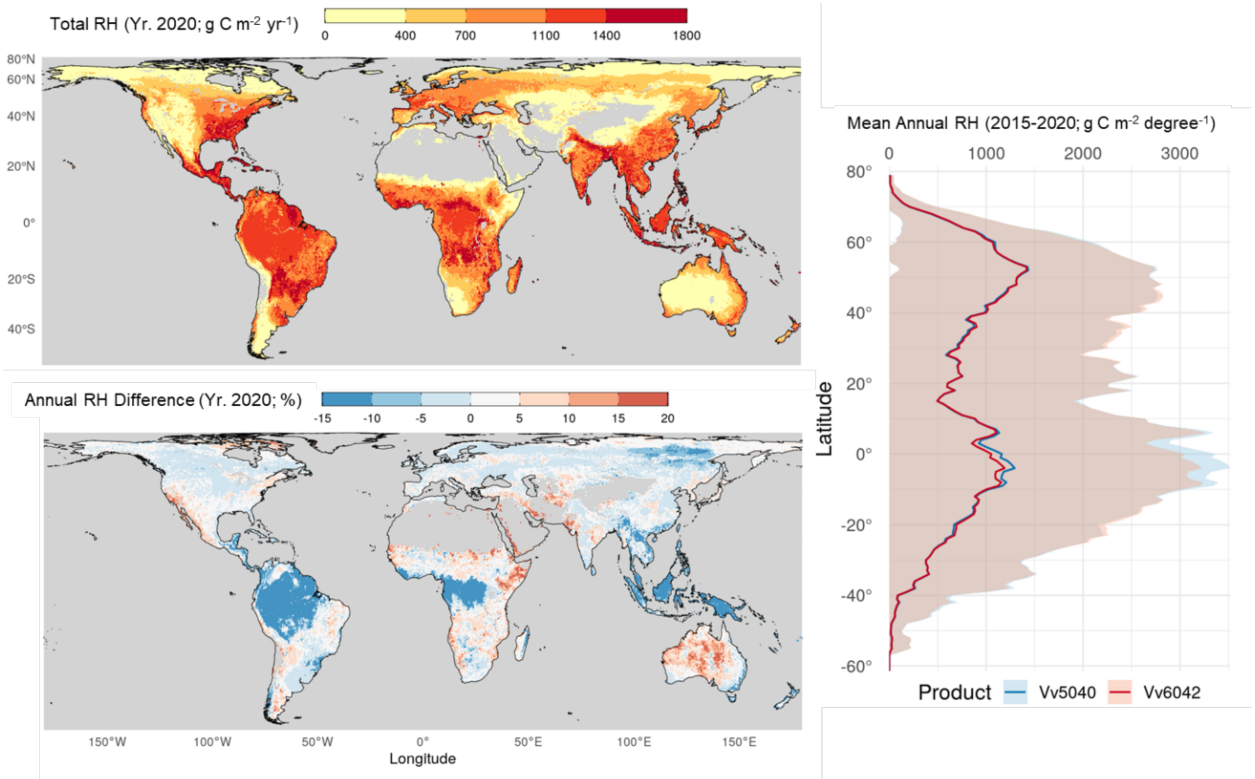

Figure 3. Global pattern of estimated annual RH for 2020 extracted from the SMAP L4_C v6 record (top left); the relative RH difference (%) between v6 and v5 records is also shown (lower left) along with the 1-degree latitude binned RH for 2015-2020 from each record (right); shading in the line plot denotes 1 spatial standard deviation of RH within each latitude bin for both records. The v6 RH pattern is largely consistent with the previous v5 record and shows only minor differences, except over tropical forests; the lower RH flux in the tropics for the v6 product reflects the model BPLUT recalibration and the resulting small reduction in SOC levels in EBF areas.

The multi-year RH seasonal patterns and magnitudes of the L4_C v6 and v5 daily records are shown in **Figure 4** for the major TransCom-3 regions. The two versions show strong consistency in their RH records, as they did for GPP (**Figure 2**). However, a small systematic RH reduction over the tropics is apparent in the v6 record, which results from the BPLUT recalibration to reduce GPP and SOC in EBF dominant areas. As with GPP, the v6 record captures expected global and seasonal behavior in RH, with no apparent artifacts or anomalous behavior. The seasonality in RH, like that in GPP, shows progressively larger seasonal amplitudes at higher latitudes and much smaller seasonality in the tropics. The daily variability in RH is also greater in areas with semi-arid climates, including Australia, South Africa and extending into more temperate domains. The RH variability is driven by intermittent rainfall and strong moisture related controls on soil decomposition and respiration processes in dryland regions.

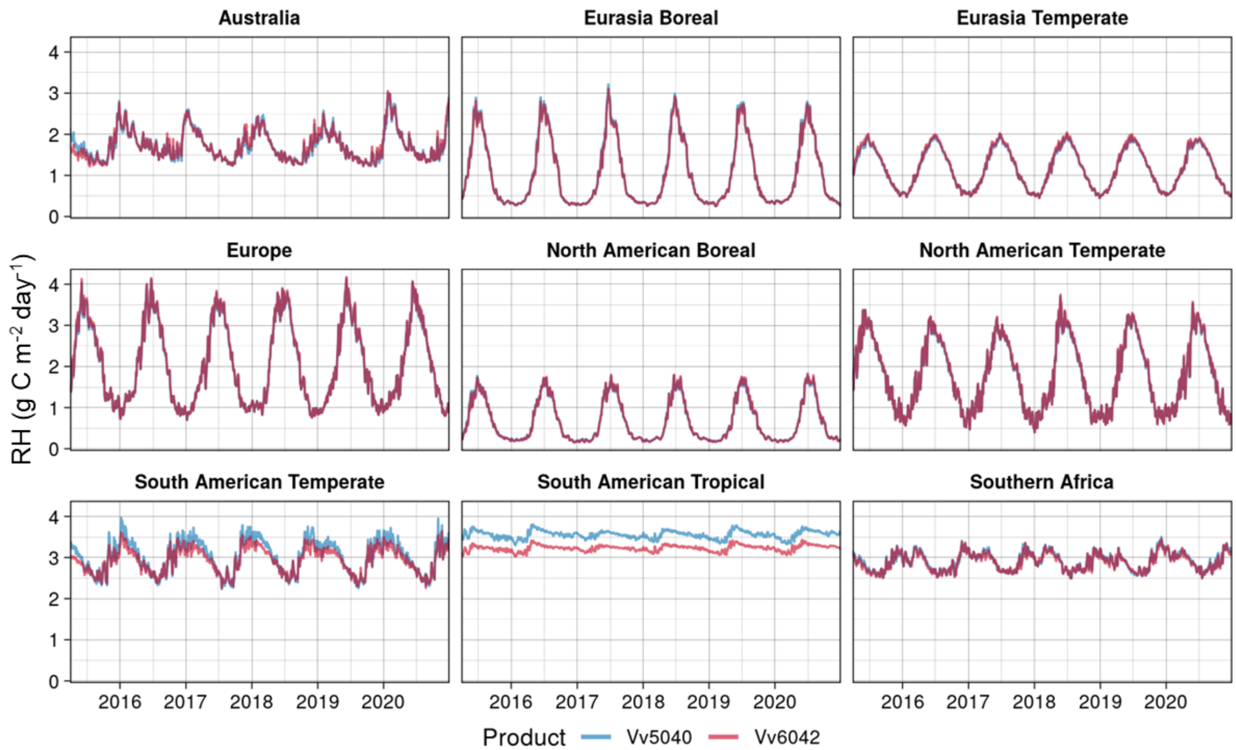

Figure 4. RH multi-year seasonal plots for the major TransCom-3 regions derived from L4_C v6 (Vv6042) and v5 (Vv5040) records. The v6 and v5 patterns are generally consistent, except for a small systematic RH difference in South American tropical and temperate regions due to the associated v6 reduction in SOC (and RH) in EBF dominant regions.

3.1.3 Net Ecosystem Exchange (NEE)

The global pattern in estimated annual net ecosystem CO_2 exchange (NEE) for 2020 is shown in **Figure 5**. In the L4_C carbon model, NEE is estimated on a daily basis as the residual difference between GPP and ecosystem respiration (RECO), where RECO is computed as the sum of RH and autotrophic respiration from vegetation growth and maintenance. Thus, the NEE pattern is affected by the magnitudes and seasonality in both GPP and respiration, and it can show variable and non-linear responses to underlying environmental trends. The annual NEE flux is the cumulative sum of the daily carbon fluxes over the calendar year and can range from positive to negative values depending on whether the ecosystem is a source or sink for atmospheric CO_2.

The NEE global pattern is very similar between the v6 and v5 records. Both records show characteristic NEE carbon sink activity over more productive regions, including wet tropical forests and croplands. While the tropics as a whole are generally close to being in balance with the atmosphere (i.e., NEE≈0), they do show significant interannual variability, including years where they act as a strong carbon sink (Le Quéré et al. 2018). Both records also show widespread NEE carbon source activity over less productive dryland regions of Australia, South Africa and western North America. However, the v6 record shows a slightly smaller and systematic NEE C-sink in the low tropics due to the model BPLUT recalibration and associated GPP and SOC reduction in EBF dominant areas.

The year 2020, depicted in the global maps, was one of the warmest years on record, with ongoing drought conditions extending across much of southern Africa and western North America. This pattern contrasts with the much wetter conditions that occurred in 2020 across China and portions of east Africa. These climate anomalies influence the NEE patterns and contribute to both stronger and weaker ecosystem carbon sources and sinks. The pattern of the ecosystem response to these anomalies is largely consistent between the v6 and v5 products.

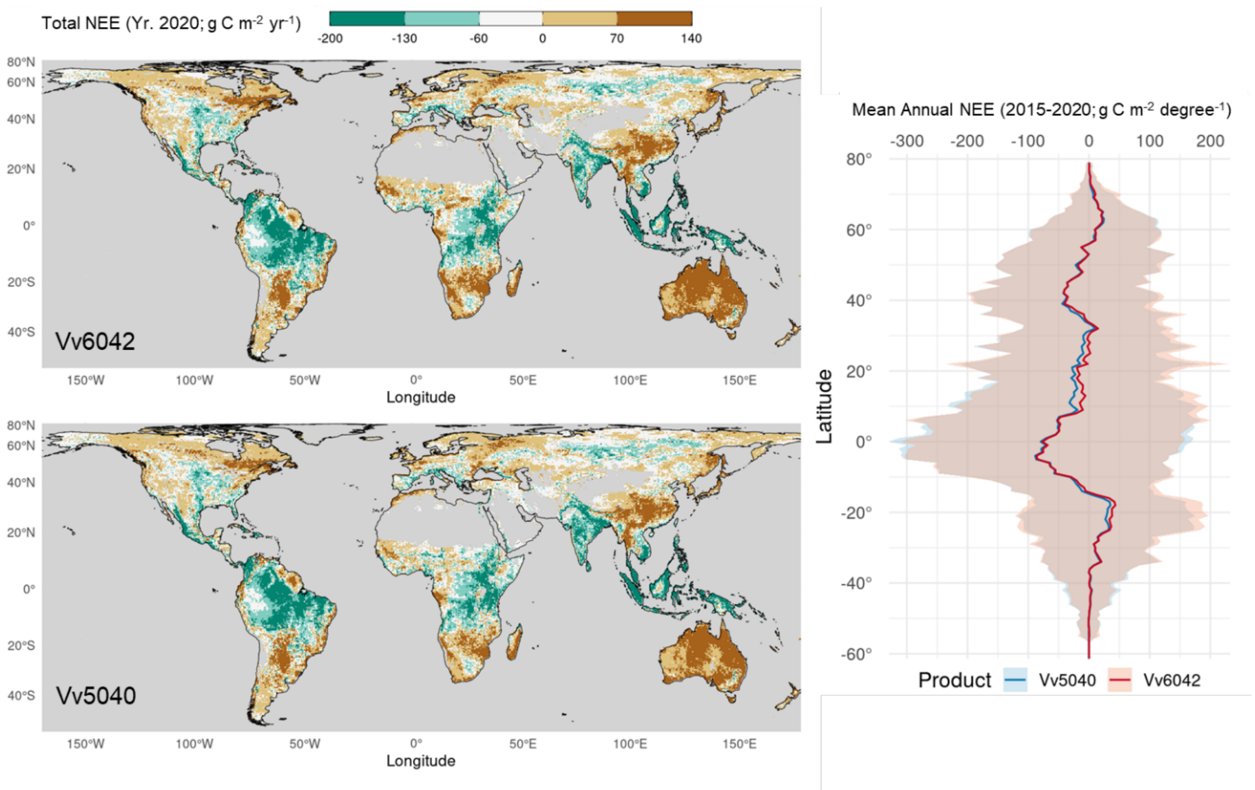

Figure 5. Comparison of L4_C estimated global patterns of annual NEE for 2020 from the latest v6 (top left) and previous v5 (lower left) records. The 1-degree latitude binned NEE means for 2015-2020 from each record are also shown (right); shading in the line plot denotes 1 spatial standard deviation of NEE within each latitude bin for both records. The v6 NEE pattern is largely consistent with the previous v5 record and shows only minor differences, including a slightly smaller NEE C-sink in the low tropics due to the model BPLUT recalibration and SOC adjustment in EBF dominant areas.

The multi-year NEE seasonal cycles from the L4_C v6 and v5 daily records are shown in **Figure 6** for the major land regions. As with the other variables, NEE generally shows a larger seasonal amplitude at higher latitudes. NEE carbon sink activity (negative flux) predominantly occurs during the growing season when conditions are suitable for vegetation growth, followed by a transition to a predominant carbon source (positive flux) regime during dormancy, major canopy disturbance events (such as wildfires or major flooding), or significant vegetation stress (such as droughts or heatwaves). Relatively large daily variability in NEE occurs in dryland regions (e.g., Australia) due to strong moisture variability and related controls on productivity and respiration. NEE also shows large daily variability in the tropics, owing to the more variable and extensive cloud cover and associated impacts on available incident solar radiation and fPAR. The large daily NEE variability in the tropics is also superimposed on a distinctive and more slowly evolving wet and dry seasonal cycle.

The NEE v6 and v5 records show good agreement. However, some minor differences do occur because of the v6 model recalibration adjustments that reduced SOC and consequently enhanced NEE carbon sink strength over EBF-dominated areas. The v6 results also show some NEE carbon sink enhancement in some dryland regions, reflecting the influence of IMERG precipitation on the L4_SM soil moisture inputs used for L4_C processing.

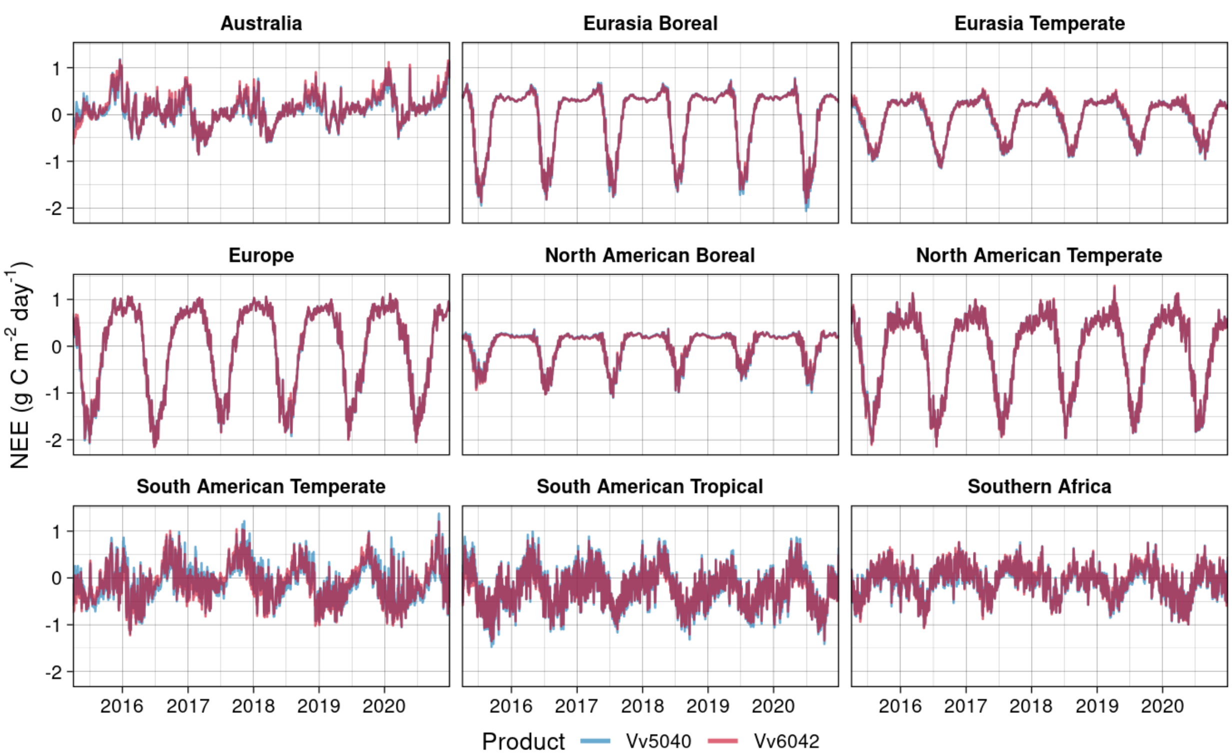

Figure 6. NEE multi-year seasonal plots for the major TransCom-3 regions derived from L4_C v6 (Vv6042) and v5 (Vv5040) records. The v6 and v5 patterns are strongly consistent due to compensating changes in the component GPP and respiration fluxes from underlying adjustments to the model calibration and environmental drivers.

3.1.4 Soil Organic Carbon (SOC)

The global pattern in estimated surface (0-5 cm depth) SOC from the L4_C v6 product for 2020 is shown in relation to the previous v5 product in **Figure 7**. The L4_C v6 product is very similar to the previous v5 product except for a small reduction in SOC stocks over EBF-dominated land areas in the tropics and a small SOC enhancement in the high latitudes. These changes are the result of model BPLUT recalibration adjustments to improve model SOC correspondence with global soil inventory data (Endsley et al. 2020). The v6 product also shows a small but widespread SOC enhancement in dryland regions including portions of central Australia, southern and east Africa, and the American southwest. These changes reflect the influence of IMERG precipitation on the L4_SM v6 soil moisture record used for L4_C processing. Overall, the resulting SOC differences between the v6 and v5 records are small, with a mean 2020 RMS difference of 0.53 kg C m^{-2} (normalized RMS difference of ~11%).

The latest L4_C v6 product preserves the characteristic SOC global patterns, including higher SOC stocks in cold, northern boreal forest and tundra biomes, which are estimated to hold more than half of the global soil carbon (Tarnocai et al. 2009). The L4_C SOC map also shows relatively high soil carbon storage in temperate forest areas due to high forest productivity rates and cool, moist soils that promote greater SOC storage. Lower SOC levels occur over dry climate zones, including desert areas in the American southwest, congruent with generally low productivity levels, warm climate conditions and associated low SOC accumulations. However, SOC levels are elevated in many dryland regions where low to moderate productivity is sufficient to generate litterfall, while strong seasonal soil moisture and temperature restrictions limit soil decomposition and promote SOC accumulation (Endsley et al. 2020). The L4_C results also show relatively low SOC levels in the wet tropics, where high GPP and litterfall rates are offset by rapid SOC decomposition and large RH emissions, so that most terrestrial carbon storage in the tropics is in vegetation biomass rather than soil (Baccini et al. 2012).

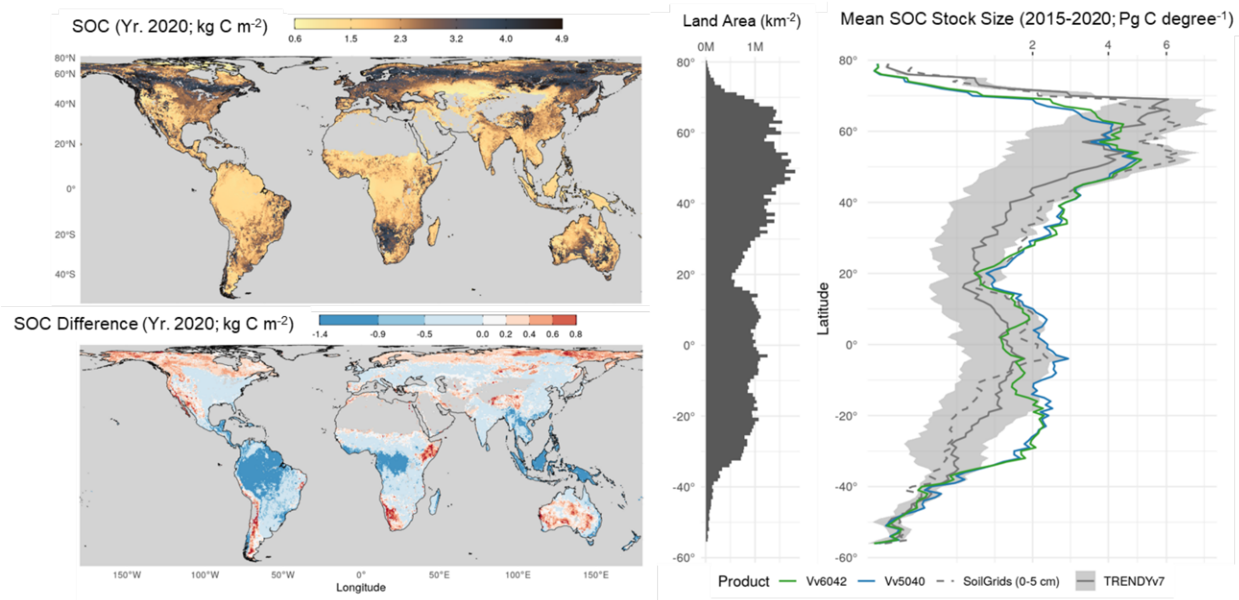

Figure 7. Global pattern in estimated surface (~0-5 cm) SOC (kg C m^{-2}) from the L4_C v6 record for 2020 (top left) and the associated difference from the previous v5 record (lower left). The SOC estimates are derived at a 1-km spatial resolution during L4_C processing and posted to a 9-km resolution global EASE v2 projection grid. Grey shading denotes barren land, permanent ice, open water and other areas outside of the model domain. A plot of the average 2015-2020 global SOC stocks within 1-degree latitude bands in relation to other independent SOC records from SoilGrids (Hengl et al. 2017) and TRENDYv7 DGVMs (Le Quéré et al. 2018) is shown on the right; grey shading in the plot denotes 1 spatial standard deviation around the TRENDY model ensemble mean, while the land area represented within each latitude bin is also shown (center).

The L4_C soil carbon product is an estimate of the SOC content in the surface (0-5 cm) soil layer. The L4_C v6 mean global SOC density map for the 2015-2020 record was aggregated to the SOC storage by latitude band and compared with other global SOC inventories in **Figure 7** after Endsley et al. (2020). The L4_C v6 results generally capture the SOC latitudinal gradient indicated from other independent SOC benchmarks represented from SoilGrids (Hengl et al. 2017) and TRENDYv7 dynamic global vegetation model (DGVM; Le Quéré et al. 2018) ensemble predictions (Pearson's r = 0.74 to 0.84 in v5; r = 0.79 to 0.88 in v6). The L4_C record slightly underestimates SOC storage in the high northern latitudes relative to the other benchmarks, which may reflect unaccounted-for deep SOC in highly organic boreal-arctic permafrost soils. The L4_C record also shows generally larger SOC storage than the other benchmarks in the extra-tropical latitudes (~20-40 degrees N/S). The larger L4_C SOC levels in these regions may reflect relatively sparse ground truth data in semi-arid dryland regions which are widespread across these latitude bands and may contribute to greater regional uncertainty in the SoilGrids and TRENDYv7 datasets. The L4_C SOC predictions also have greater uncertainty in these regions for similar reasons, so further investigation may be needed to clarify SOC distributions and associated product accuracy within these latitude bands.

The multi-year seasonal patterns and magnitudes in the estimated surface SOC stocks from the L4_C v6 and v5 daily records are compared in **Figure 8** for the major TransCom-3 land regions.

Both records show very similar magnitudes and relative differences in SOC storage by region. Both records also show strong consistency in reproducing the subtle seasonal variations in soil carbon storage resulting from lags between vegetation growth and litterfall inputs, on the one hand, and soil decomposition and respiration losses, on the other. Both records show general SOC stability over the multi-year record, with no indication of anomalous artifacts. However, both records also show positive trends in soil carbon storage in most regions stemming from environmental trends represented in the L4_C model inputs. The SOC trends are small (i.e. <0.03 kg C m^{-2} yr^{-1}) relative to the estimated soil carbon storage, but may partially reflect climatology differences between the daily meteorology inputs from the MERRA-2 (GEOS 5.12.4) and GEOS Forward-Processing[‡] (GEOS 5.13.1-GEOS 5.27.1) products that are used for L4_C initialization and operations, respectively (Kimball et al. 2014). While both L4_C product versions are very similar, there are notable v6 differences from the prior v5 product release, including a systematic SOC reduction over the tropics and a small SOC increase over the boreal regions.

[‡] https://gmao.gsfc.nasa.gov/GMAO_products/NRT_products.php

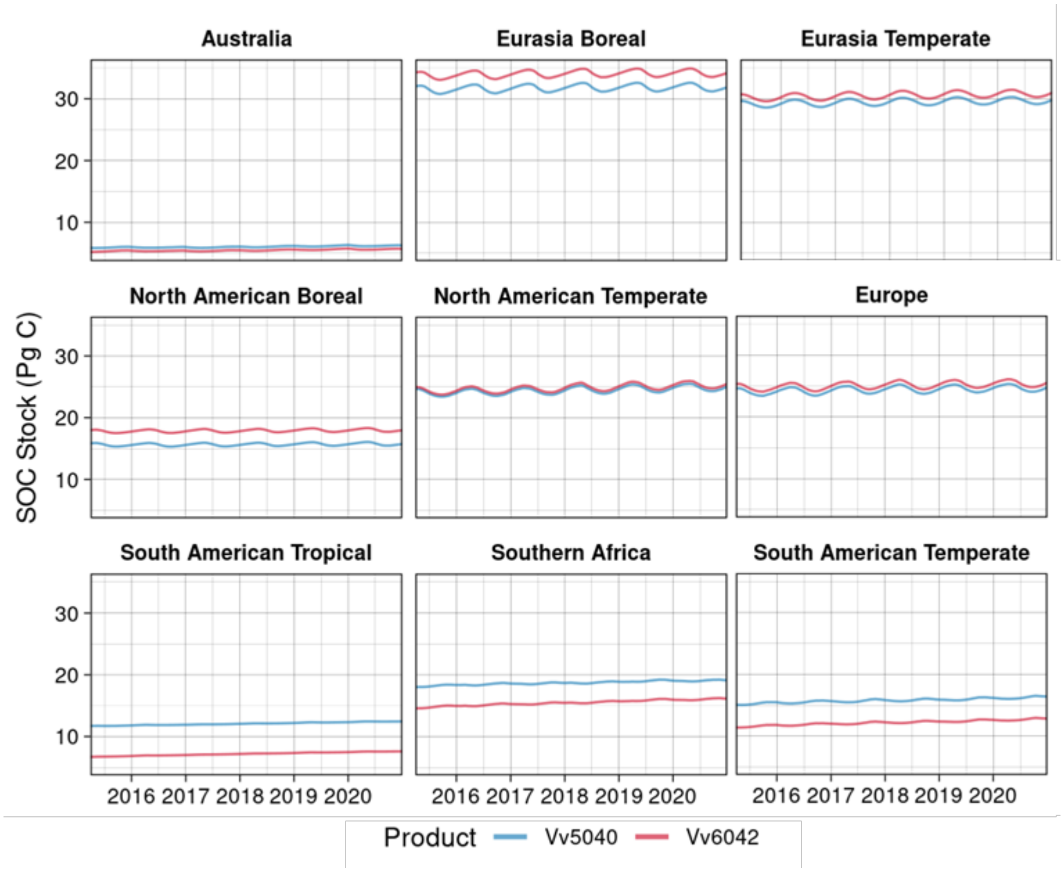

Figure 8. Multi-year seasonal plots of estimated surface (0-5 cm) SOC stocks for the major TransCom-3 regions derived from L4_C v6 (Vv6042) and v5 (Vv5040) records. The v6 and v5 patterns show overall consistency, but with small systematic v6 reductions in the tropics and some SOC enhancement in boreal regions stemming from the model recalibration. Both SOC records show similar stability over the long-term record, but with small positive annual storage trends imposed from the model environmental inputs.

3.2 Influence of different L4_SM precipitation forcings on L4_C v6 performance

The SMAP L4_SM product provides daily soil moisture and soil temperature inputs to the L4_C algorithm to derive associated environmental controls on estimated carbon fluxes. The L4_C v6 processing obtains these critical inputs from the latest L4_SM v6 product, which includes an improved precipitation forcing applied in the land modeling system (Reichle et al. 2022). The precipitation forcing used in L4_SM v6 primarily utilizes satellite- and gauge-based IMERG products and thus differs from the gauge-only precipitation forcing used in L4_SM v5. Two different IMERG products are used for L4_SM v6 processing due to the different latencies of these products and their influence on SMAP operational processing. The IMERG-Final product is derived from both satellite observations and cumulative monthly measurements from global precipitation gauges and has a ~3.5-month latency; the IMERG-Late product is derived solely from satellite observations and has a much shorter (~14-hour) latency. A change in the L4_SM Science

Version ID from Vv6032 to Vv6030 on data-day 30 June 2021 indicates the switch from IMERG-Final to IMERG-Late inputs. These changes coincide with corresponding L4_C Science Version ID changes from Vv6042 to Vv6040 for the same period.

The resulting impact of the change in L4_SM precipitation forcings on the L4_C product is expected to be small given the documented low level impact of this change on L4_SM performance (Reichle et al. 2022). This is confirmed by the general consistency between L4_C v6 and v5 records summarized above (4.1). We also investigated potential differences in L4_C time-series spanning the 30 June, 2021 transition date between the L4_C Vv6042 to Vv6040 portions of record. As illustrated in **Figure 9** for a selection of FLUXNET tower locations, the Vv6042 and Vv6040 carbon flux records show overall consistency with each other and with the previous L4_C v5 (Vv5040) record.

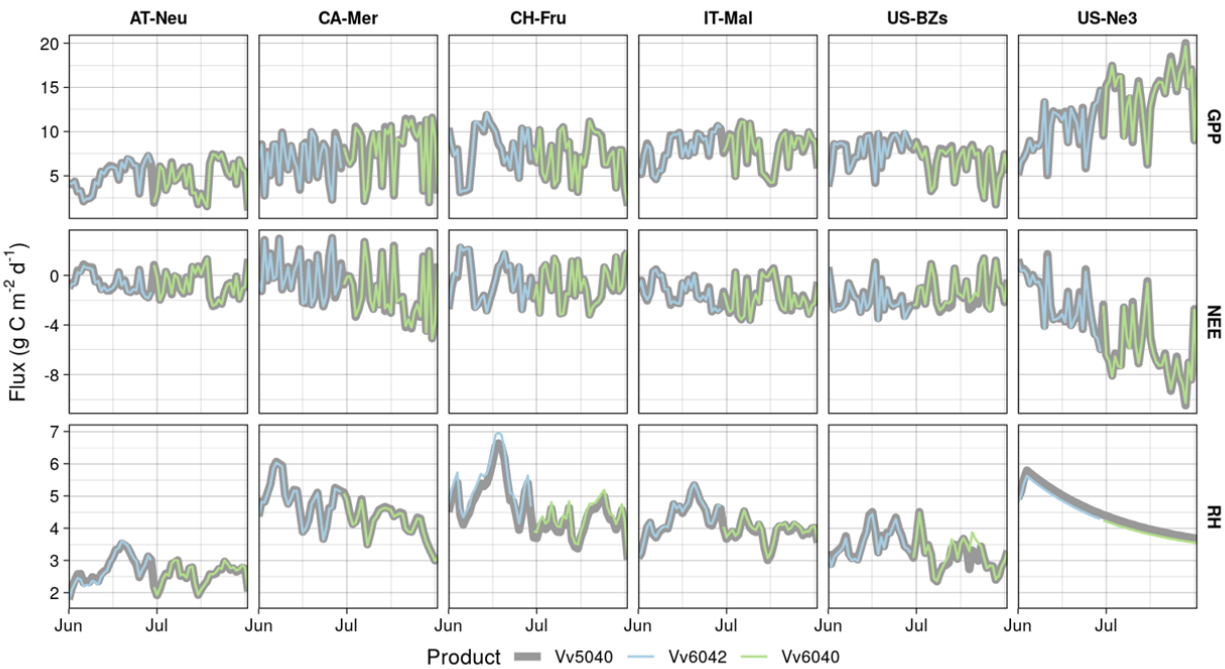

Figure 9. Estimated L4_C daily gross primary production (GPP), net ecosystem exchange (NEE) and heterotrophic respiration (RH) for a global selection of FLUXNET sites representing temperate grassland (AT-Neu, CH-Fru, IT-Mal), boreal peatland (CA-Mer), boreal forest (US-BZs) and cropland (US-Ne3). The plots cover the two-month period spanning the transition from Vv6042 (blue line) to Vv6040 (green line) portions of the L4_C v6 record on data day 30 June, 2021. The v6 results are also compared with the L4_C v5 operational record (in grey). The latest v6 time series show general consistency with each other and with the previous v5 record, with no indication of anomalous artifacts imposed from the different precipitation forcings used in the upstream L4_SM processing.

3.3 VIIRS fPAR impact on L4_C performance

The L4_C processing uses daily fPAR inputs derived from ancillary satellite observations as key model inputs for estimating GPP and litterfall (Kimball et al. 2014). Currently, daily fPAR is interpolated from 8-day composite fPAR estimates from the MOD15A2H product, which is based on MODIS observations from the NASA EOS Terra satellite. However, the Terra satellite has far exceeded its original design life and will soon cease making science-quality observations owing to orbital decay and diminishing fuel reserves. The NASA Aqua satellite is also approaching the end of its effective mission life, jeopardizing the use of alternative operational fPAR products from the Aqua MODIS sensor. It is projected that by Fall 2022, the Terra satellite's mean local equatorial crossing time will be at least 15 minutes earlier than initially designed. As this crossing time shifts earlier, gradual differences in illumination angle could begin to impact product quality. Consequently, planning for the migration of fPAR inputs from MODIS to VIIRS began as part of the L4_C v6 development. The VIIRS instruments onboard the Suomi National Polar-orbiting Project (NPP) and Joint Polar Satellite System (JPSS) satellites have spectral bands similar to MODIS, and the VIIRS VNP15A2H fPAR operational product is designed for compatibility with the MODIS fPAR record (Xu et al. 2018). Moreover, VNP15A2H data granules have the same spatial resolution and spatial reference system (SRS) as MOD15A2H data granules, with global coverage. This makes VIIRS fPAR a suitable replacement for MODIS fPAR in global applications. However, the data products do have some differences in formatting and quality assurance (QA) information that require modifications to the L4_C processing system.

The QA information provided from the fPAR products is used in the L4_C algorithm to identify and screen out lower quality fPAR grid cell values, which are replaced with alternative collocated "clear-sky" values from an ancillary 8-day fPAR global climatology in preprocessing (Kimball et al. 2014). However, whereas the MOD15A2H granules report cloud cover and retrieval quality information in a single QA band, the VNP15A2H granules report this information in two different QA bands, including one that has a superficial resemblance to the single band in MOD15A2H. The bit-packing of the QA flags in that band, however, are different. Moreover, the classification of cloud status is different between MOD15A2H and VNP15A2H: whereas the former describes cloud cover in terms of "significant clouds [were/ were not] present," "mixed clouds present," and "cloud state not defined," the latter product describes cloud status in probabilistic terms only, with QA values ranging from "confident clear," "probably clear," "probably cloudy," to "confident cloudy." To address the above QA differences between fPAR products, we developed a cross-walk table, in combination with expert judgement, to convert VIIRS fPAR QA values to the baseline MODIS fPAR QA values used for L4_C processing. The L4_C model operation using the alternative VIIRS fPAR input data was tested and is now ready to be enabled in a future product release or earlier in case of an unexpected interruption in the Terra MODIS product stream.

VIIRS fPAR retrievals are likely to have lower-quality in humid tropical regions due to the afternoon overpass time (1330 local time) of the JPSS VIIRS satellite, compared with the morning overpass of Terra (originally 1030 local time). However, the VIIRS and MODIS fPAR records are considered generally consistent (Xu et al. 2018, Yan et al. 2021). Initial testing of the L4_C operational code with VIIRS fPAR inputs was successful and confirmed the expected impact of switching to VIIRS fPAR. **Figure 10** shows that, for a single data day, the impact on GPP from switching to VIIRS fPAR is on the order of ±1 g C m^{-2} d^{-1} in the most productive regions (e.g., during summer in the northern hemisphere) and is much smaller elsewhere. Downstream effects on other L4_C carbon variables are generally smaller. These minor impacts from the fPAR sources reflect the associated differences in satellite overpass times, sensor characteristics, retrieval algorithms, and QA criteria between MODIS and VIIRS. The resulting low impact of the VNP15A2H inputs on L4_C performance and the similar latency of both fPAR products indicates that the VIIRS fPAR record is well suited for L4_C operations.

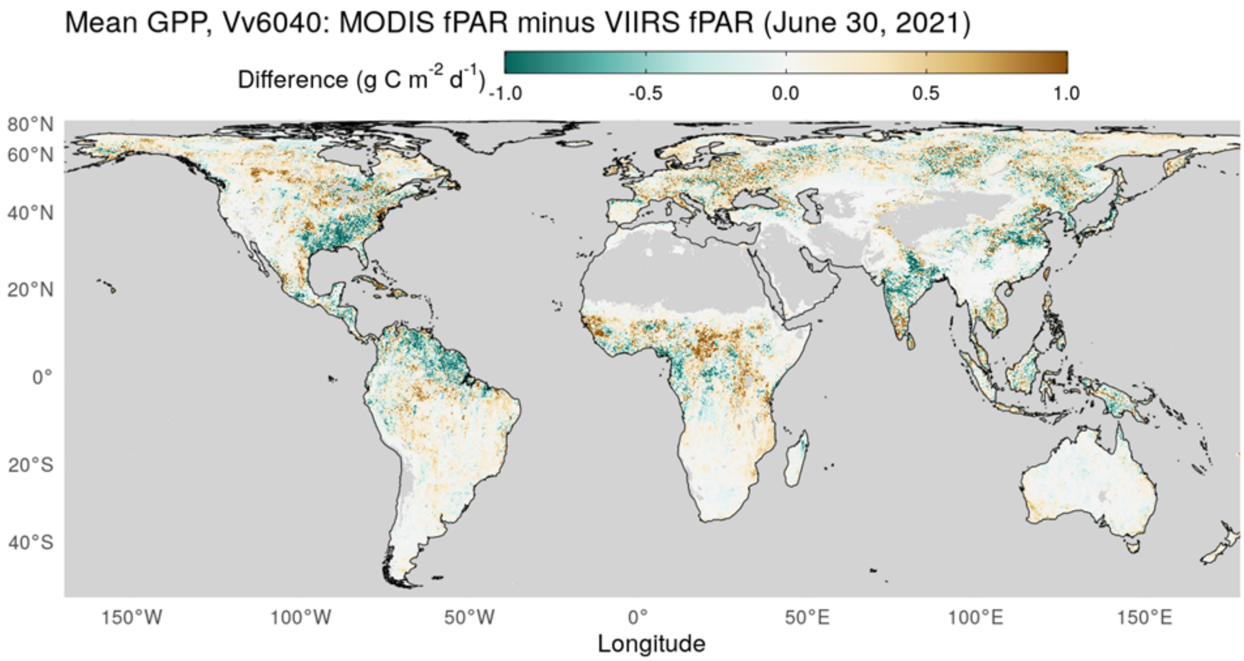

Figure 10. Difference in L4_C GPP for a selected data day near the peak of the Northern Hemisphere growing season, based on using MODIS fPAR or VIIRS fPAR. Negative values (green) show areas estimated to be more productive (higher GPP) using VIIRS fPAR instead of MODIS fPAR, whereas positive values (brown) indicate areas estimated to be less productive.

3.4 L4C performance against tower CVS observations

The L4_C v6 daily carbon fluxes for NEE, GPP and RECO (derived as the daily sum of RH and autotrophic respiration) were compared against in situ measurements from eddy covariance towers at 26 L4_C core validation sites (CVS) over the available three-year (2015-2017) CVS record. The v6 performance was also assessed in relation to the L4_C v5 record, the assessment including comparisons with the L4_C Nature Run (NR) records pertaining to the latest v6 (NRv9.1) and previous v5 (NRv8.3) product releases. The NR records are derived without the direct influence of assimilated SMAP brightness temperatures in the L4_SM algorithm and provide a means to assess the evolution in model performance without the benefit of SMAP observations. Differences in L4_C accuracy among the four product sets (NRv8.3, NRv9.1, L4_C v5, and L4_C v6) relative to the independent CVS observational benchmark provide a measure of potential gains in product accuracy over earlier product releases (v6 compared to v5) and from the SMAP operational data assimilation (v6 compared to NRv9.1). Primary metrics used for the CVS comparisons included the Pearson correlation and root mean squared error (RMSE) vs. tower measurements.

Unlike the historical FLUXNET tower eddy covariance records used for the model BPLUT calibration, the CVS observations used in this L4_C accuracy assessment are independent of the L4_C model and available during the SMAP operational record. The SMAP L4_C CVS sites are summarized in **Table 1**, and the CVS locations are presented in **Figure 11**, along with the larger global set of FLUXNET (La Thuile and FLUXNET2015) tower sites used for the L4_C model calibration (Jones et al. 2017).

Table 1. CVS sparse tower network used for L4_C product validation assessments.

[1]Site	[2]PFT	Lat	Lon	Location	Full Name
FI-Sod	ENF	67.36	26.64	Finland	FMI Sodankyla
CA-Oas	ENF	53.99	-105.12	Sask. CN	BERMS Southern Old Black Spruce
US-ICt	SHR	68.61	-149.30	AK, USA	Imnavait Tussock
US-ICh	SHR	68.61	-149.30	AK, USA	Imnavait Heath
US-ICs	SHR	68.61	-149.31	AK, USA	Imnavait Wet Sedge
US-BZs	ENF	64.70	-148.32	AK, USA	Bonanza Creek Black Spruce
US-BZb	ENF	64.70	-148.32	AK, USA	Bonanza Creek Bog
US-BZf	ENF	64.70	-148.31	AK, USA	Bonanza Creek Fen
US-PFa	DBF	45.95	-90.27	WI, USA	Park Falls
US-Atq	GRS	70.47	-157.41	AK, USA	Atqasuk
US-Ivo	SHR	68.49	-155.75	AK, USA	Ivotuk
US-SRM	SHR	31.82	-110.87	AZ, USA	Santa Rita Mesquite
US-Wkg	GRS	31.74	-109.94	AZ, USA	Walnut Gulch Kendall Grasslands
US-Whs	SHR	31.74	-110.05	AZ, USA	Walnut Gulch Lucky Hills Shrubland
US-Ton	SHR	38.43	-120.97	CA, USA	Tonzi Ranch
US-Var	SHR	38.41	-120.95	CA, USA	Vaira Ranch
AU-Whr	SHR	-36.67	145.03	Australia	Whroo
AU-Rig	CRP	-36.66	145.58	Australia	Riggs Creek
AU-Ync	CRP	-34.99	146.29	Australia	Yanco
AU-Stp	GRS	-17.15	133.35	Australia	Sturt Plains
AU-Dry	GRS	-15.26	132.37	Australia	Dry River
AU-DaS	GRS	-14.16	131.39	Australia	Daily River Savannah
AU-How	GRS	-12.50	131.15	Australia	Howard Springs
AU-GWW	SHR	-30.19	120.65	Australia	Great Western Woodlands
AU-ASM	SHR	-22.28	133.25	Australia	Alice Springs
AU-TTE	SHR	-22.29	133.64	Australia	Ti Tree East

[1]FLUXNET-based tower site identifiers; [2]Tower PFT classes defined from a 1-km resolution MODIS (MOD12Q1) Type 5 (8 vegetation class) global land cover map, consistent with L4_C processing.

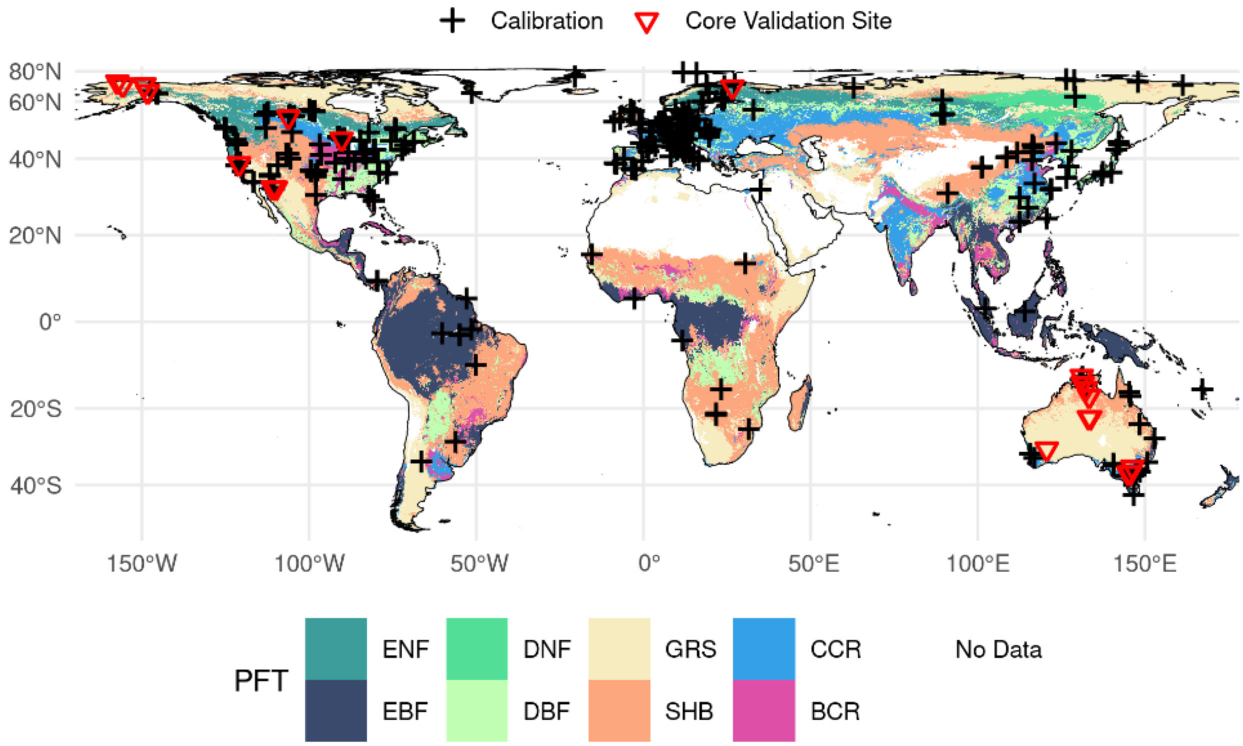

Figure 11. CVS locations used for L4_C product validation. FLUXNET sites with historical tower records used for the L4_C model calibration are also shown in relation to global plant functional types summarized from the MODIS MOD12Q1 (8 vegetation class) global land cover classification (Friedl et al. 2010).

The correlation and RMSE metrics of the simulated daily carbon fluxes (NEE, GPP and RECO) are shown in **Figure 12**, averaged over the CVS sites. The three-year (2015-2017) evaluation period is defined by the overlap between SMAP operations and the 26 CVS tower site records. The results show meaningful improvement in v6 performance over the v5 record for NEE, indicated by higher correlations and lower RMSE values relative to the independent CVS observations. Both L4_C operational products (v6 and v5) also show better performance than their model-only Nature Run records (NRv9.1 and NRv8.3) for NEE, indicating a clear benefit of the SMAP observations on L4_C accuracy. The latest model-only (NRv9.1) results are also improved over the prior NRv8.3 release, indicating continued advancements in the modeling framework. The v6 NEE results also remain well within the targeted L4_C performance threshold (mean NEE RMSE $\leq$ 1.6 g C m^{-2} d^{-1}), indicating that the product performance is robust at the level of tower observation uncertainty (Baldocchi et al. 2008).

The L4_C performance assessment for RECO is similar to that for NEE in showing meaningful v6 improvement over the previous v5 record. In contrast, the v6 GPP record shows no meaningful RMSE reduction and an only slightly stronger correlation with the CVS observations compared to the v5 record. The favorable performance and systematic improvements seen for NRv9.1 also demonstrate that the L4_C carbon model and GEOS land model assimilation framework continue to advance and produce science quality data.

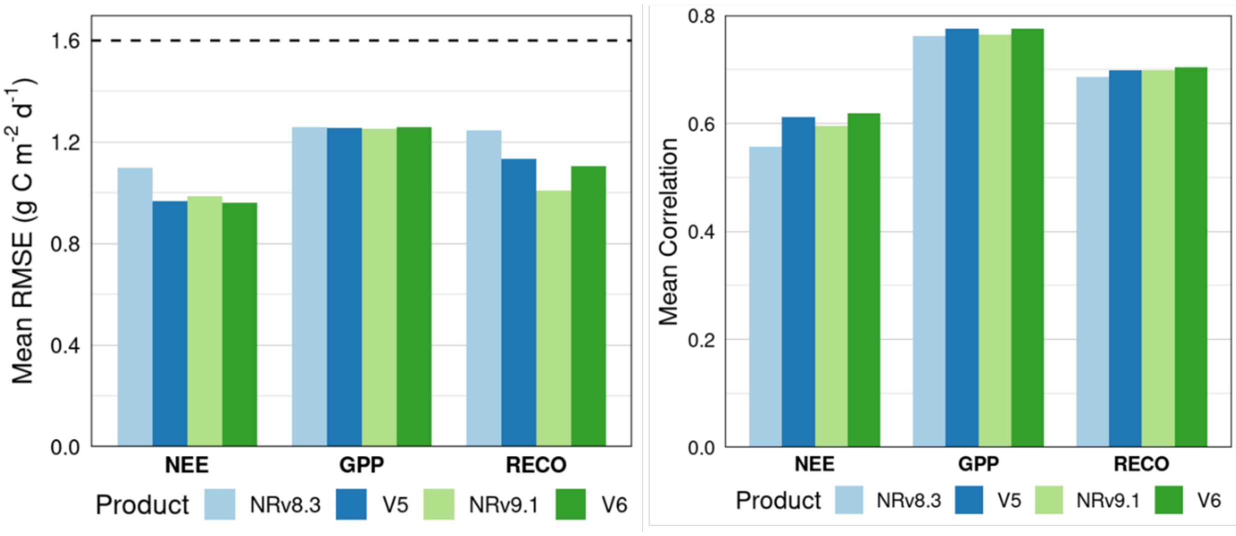

Figure 12. Summary of global CVS comparisons between daily tower observations and L4_C estimates of NEE, GPP and RECO for 2015-2017; reported metrics include mean RMSE and correlations across the 26 sites. L4_C outputs include the latest v6 operational product, the previous v5 product, and the associated model Nature Run outputs for v6 (NRv9.1) and v5 (NRv8.3). The targeted daily NEE RMSE threshold for the L4_C product (1.6 g C m^{-2} d^{-1}) is denoted by the horizontal dashed line in the left panel.

3.5 L4_C consistency with other global carbon products

Following Jones et al. (2017), the L4_C product outputs were further evaluated against independent global carbon products, including:

1.) FLUXNET machine-learning upscaled global carbon fluxes from the FLUXCOM initiative, derived using the "remote sensing plus meteorological/climate forcing" (RS+METEO) setup (Jung et al. 2020), and
2.) Solar-Induced chlorophyll Fluorescence (SIF) data derived from OCO-2 (Orbiting Carbon Observatory) satellite observations (Zhang et al. 2018).

The objective of these comparisons was to assess and document the general consistency of selected L4_C product fields with similar parameters derived from independent information about global carbon fluxes and productivity.

The global comparisons spanned four complete annual cycles (2016-2019) within the SMAP operational record. The comparison was limited to the available overlapping record between SMAP operations and the benchmark datasets. The period used for evaluation was also distinct from that of the L4_C BPLUT calibration (section 2). The FLUXCOM data provide global extrapolations of daily NEE and GPP that extend well beyond the limited tower eddy covariance sampling footprints represented by the CVS comparison, while effectively integrating the extensive FLUXNET global tower observational record with other synergistic remote sensing and surface meteorological information within an ensemble machine learning model extrapolation framework; these data were used to verify regional patterns, seasonal behavior, and interannual variability in the L4_C carbon flux record. Composited monthly and annual SIF observations from the Orbiting Carbon Observatory (OCO-2) were also used as an observational proxy for GPP (Li et al. 2018) and provided an additional check on the global pattern and seasonal variability in L4_C GPP (Zhang et al. 2018; Li et al. 2020). Detailed summaries of these comparisons are provided below.

3.5.1 FLUXCOM

The FLUXCOM "RS+METEO" record used here is derived using an ensemble of three machine learning methods and five global climate forcing datasets for empirical upscaling of tower-based daily carbon flux observations from the global FLUXNET data archive (Jung et al. 2020). The spatial upscaling approach also uses other explanatory geospatial variables from mean seasonal cycles of satellite data and daily meteorology observations. The FLUXCOM data are available on a 0.5-degree resolution global grid, whereas the L4_C product is produced in a finer 9-km resolution global EASE-grid 2.0 format. For the comparison, the L4_C and FLUXCOM data were spatially aggregated and compared over a consistent set of TransCom-3 global land regions (Baker et al., 2006). While FLUXCOM is not necessarily more or less accurate than L4_C, it represents a different method for upscaling the same observed flux tower data (i.e., same training data), so we would expect broad agreement between the flux estimates.

The multi-year seasonal variations in estimated NEE and GPP for the major land regions from the overlapping L4_C (v6 and v5) and FLUXCOM records are presented in **Figure 13**. Grey shading in the figure denotes ±1 standard deviation for the FLUXCOM values across each sub-region as a rough measure of uncertainty. Overall, the results show nearly identical behavior between the L4_C v6 and v5 products across all global sub-regions and over the multi-year record. The L4_C results also show favorable correspondence with the FLUXCOM record in capturing the regional magnitudes and multi-year seasonal cycles in both GPP (median r=0.97, RMSD[§]<1.01 g C m^{-2} d^{-1}) and NEE (median r=0.78, RMSD<1.32 g C m^{-2} d^{-1}), but with larger NEE regional mean difference over tropical and temperate South America, and Southern Africa. The relative agreement between L4_C and FLUXCOM mean carbon fluxes across each sub-region is generally within the range of uncertainty (grey shading). The relative agreement is also stronger for GPP due to its larger seasonal amplitude and the greater inherent uncertainty in NEE, which is derived as a residual difference between much larger GPP and RECO fluxes. While the L4_C and FLUXCOM results show generally favorable correspondence, some systematic regional differences are apparent. For example, the L4_C results show less NEE carbon sink strength over South America and Southern Africa due to a larger L4_C respiration flux relative to FLUXCOM. Here, the FLUXCOM uncertainty is also larger, which partly reflects the lack of flux tower observations in these regions (Schimel et al. 2015).

[§]Root-mean-square difference.

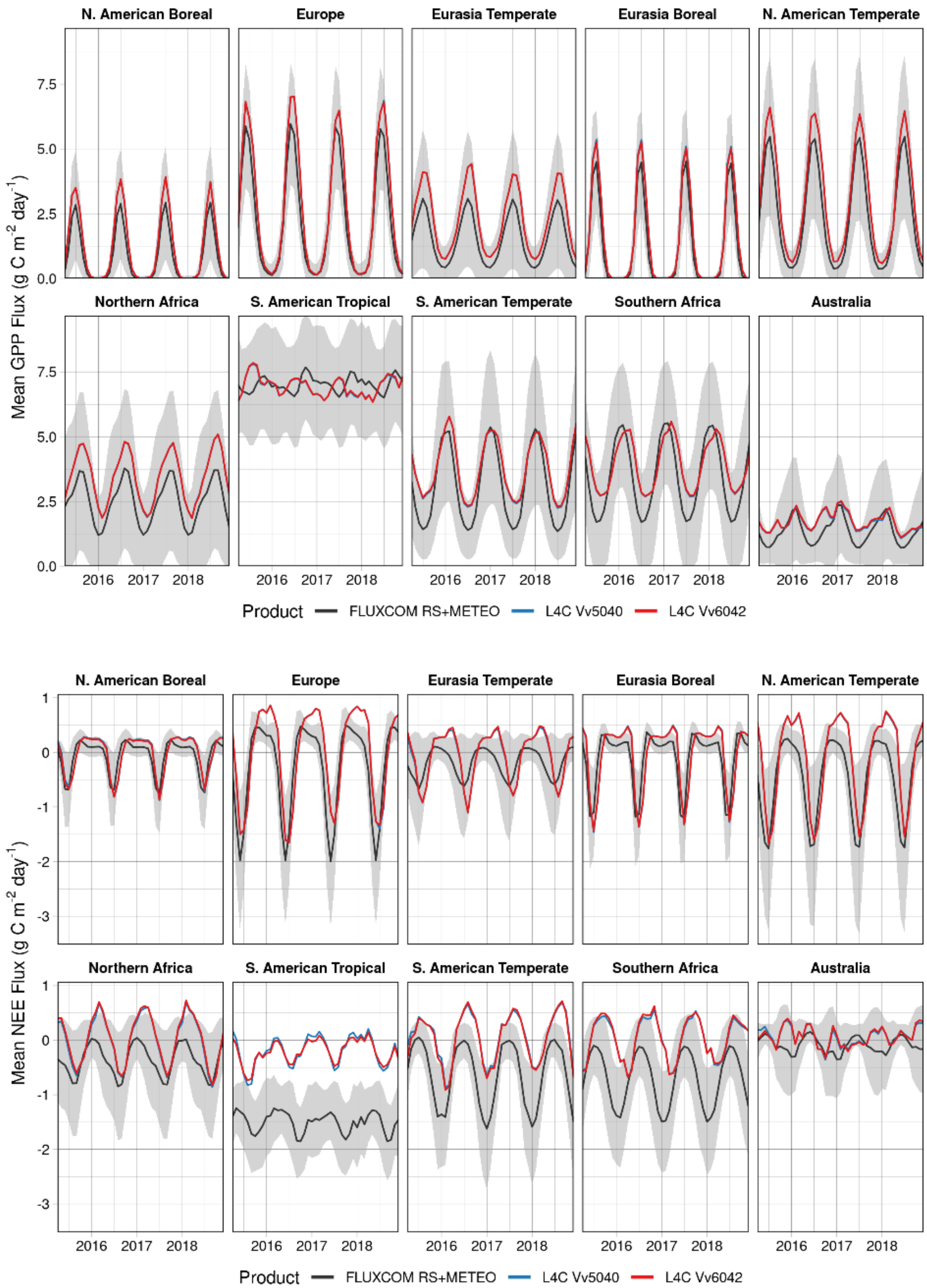

Figure 13. Mean daily (top) GPP and (bottom) NEE from the SMAP L4_C and FLUXCOM global data products aggregated over the major TransCom-3 regions. The FLUXCOM mean daily carbon fluxes are shown by the black lines. The grey shading indicates ±1 standard deviation of the FLUXCOM values across each sub-region. The L4_C mean daily outputs from the current v6 (Vv6042) and prior v5 (Vv5040) product releases are shown by the respective red and blue lines.

3.5.2 Satellite SIF observations

The global patterns in mean annual productivity indicated from the L4_C v6 GPP and OCO-2-derived SIF records are shown in **Figure 14**. The global, spatially continuous SIF (CSIF) data used for this comparison are provided at 0.05-degree spatial and 4-day temporal resolution and were derived from a neural network trained on OCO-2 SIF measurements at the 737 nm spectral wavelength (Zhang et al. 2018). For this comparison, the CSIF data were re-projected to the 9-km resolution global EASE-Grid version 2.0 of the L4_C product using nearest-neighbor resampling, and the L4_C GPP and CSIF records were further composited into monthly data. Since SIF is a byproduct of plant photosynthesis, the data are normalized to account for global variations in photosynthetically active radiation (PAR). SIF (mW m^{-2} sr^{-1} nm^{-1}) is generally proportional to GPP (g C m^{-2} d^{-1}), but the relationship can vary for different PFT classes and environmental conditions (Porcar-Castell et al. 2014; Li et al. 2018). However, both the CSIF and L4_C GPP results show a similar global pattern of mean annual productivity (**Figure 14**). Both products show the greatest productivity in wet tropical forests and lowest productivity in the polar climate and arid desert regions. Both products also show similar intermediate levels of productivity in temperate forests and agricultural regions.

A plot of the mean r^2 correspondence in global productivity between the monthly 2016-2019 L4_C v6 GPP and CSIF records is also presented in **Figure 14**. This comparison is predicated on the assumption that SIF is proportional to GPP via a PFT-dependent light use efficiency (LUE) factor. Here, we multiplied the CSIF record with this PFT-dependent factor prior to computing the spatio-temporal correspondence (r^2) between these two datasets. The line plot in **Figure 14** shows the r^2 values for each calendar month, and the horizontal bars show the spread (minimum to maximum) in monthly r^2 values across the overlapping years of record. Based on the global relationship, the L4_C v6 GPP explains more than 80 percent of the variance in monthly CSIF-derived GPP. The global correspondence is slightly lower during the Northern Hemisphere summer months due to the much larger area of active vegetation growth compared to the winter months when vegetation is largely dormant over the northern temperate and high latitudes. The CSIF product also likely fills in data (using a trained neural network) more frequently in the winter months, when the signal-to-noise ratio of the underlying OCO-2 SIF retrievals is lower. The warmer summer months also coincide with greater variability in productivity due to heat and moisture related stress, which can alter the relationship between SIF and GPP, and reduce the correspondence.

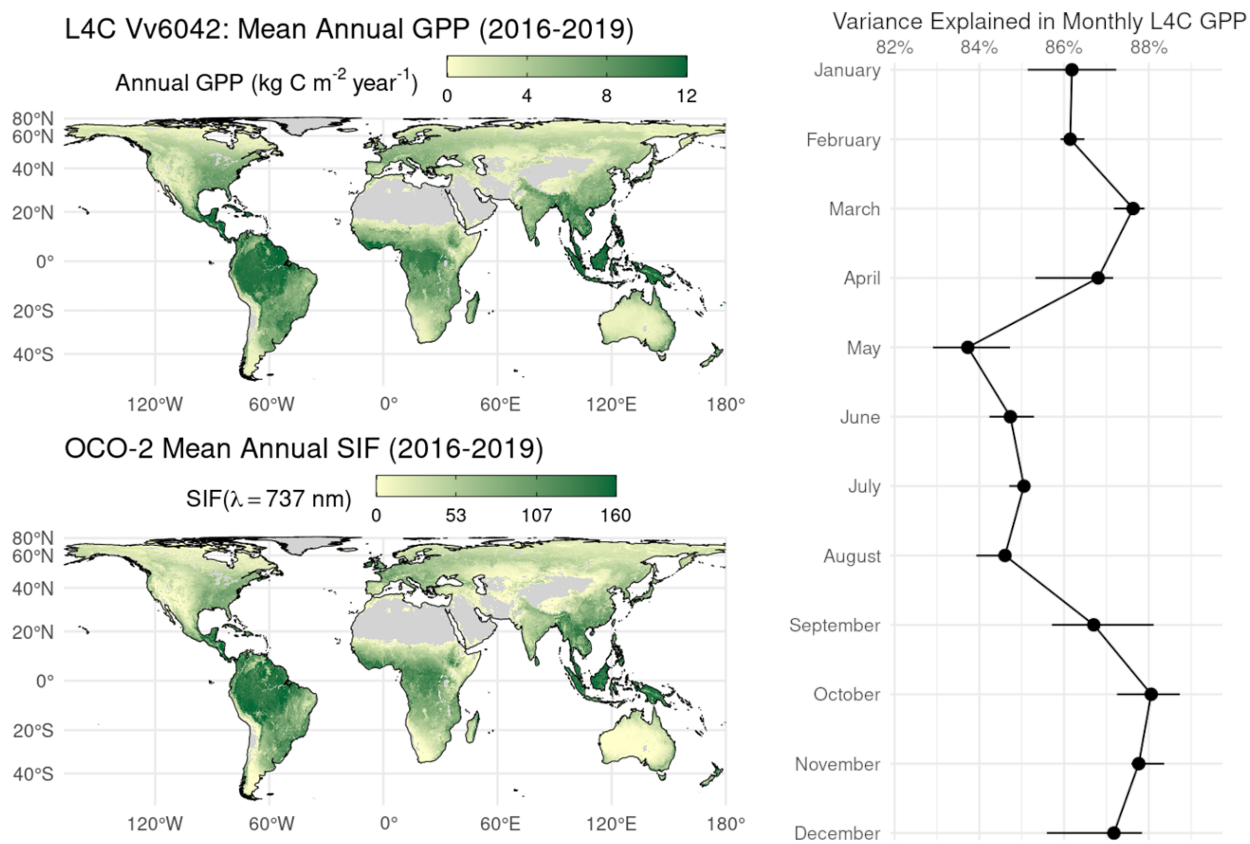

Figure 14. Comparison of global patterns of mean annual productivity indicated from the SMAP L4_C v6 (Vv6042) GPP and OCO-2-derived SIF (CSIF) records for 2016-2019 (left). The line plot (right) shows the Coefficient of Determination (r^2) between L4_C and CSIF-derived global, monthly GPP records; dots show the median r^2 correspondence (the average of the two middle r^2 values of the four values computed, one for each year) and horizontal lines denote the min-max spread in the monthly spatial correspondence over the global domain and four-year evaluation period.

3.6 Summary

This report provides an assessment of the latest (v6) SMAP L4_C product release. Methods used to ascertain the v6 product quality and performance involved: 1) qualitative evaluations of the degree to which selected product fields represent characteristic global patterns and magnitudes in terrestrial carbon fluxes and surface SOC stocks; 2) an assessment of the difference in these fields between the latest (v6) L4_C product and the previous (v5) product release; 3) validation of daily product carbon (CO_2) flux outputs against eddy covariance tower measurements from a global network of core validation sites (CVS); and 4) consistency checks of L4_C product fields against similar parameters obtained from other global benchmark datasets, including: SOC from SoilGrids and TRENDY DGVMs; FLUXCOM GPP and NEE daily fluxes; and composited monthly SIF derived from OCO-2 observations.

Based on these assessments, the L4_C v6 product continues to show a level of performance and accuracy consistent with the algorithm and product design. The product shows the expected characteristic global patterns and seasonality in estimated carbon fluxes and SOC stocks, with no apparent artifacts or anomalous behavior. The product continues to meet or exceed the targeted accuracy requirements for NEE (mean RMSE $\leq$ 1.6 g C m^{-2} d^{-1}) and continues to show favorable accuracy for GPP and RECO, with similar or better performance than the previous v5 record in relation to CVS observations. The latest v6 product also continues a pattern of meaningful and regular improvements over earlier L4_C product releases. The major L4_C product fields are generally consistent with similar variables obtained from a diverse set of global environmental benchmark data. The latest L4_C v6 product replaces earlier (v5 and older) product versions. Therefore, blending of data from the different product versions is not recommended to avoid the risk of introducing artifacts or other errors imposed from underlying differences in model parameters, model calibration, and forcing data. The L4_C product continues to be well suited for a diversity of science applications as demonstrated in previous studies, including regional and global assessments of ecosystem productivity, soil carbon, and terrestrial carbon sink activity (Jones et al. 2017, Endsley et al. 2020), agricultural assessments of crop conditions and annual crop yields (e.g. Wurster et al. 2020), and assessments of regional drought impacts and environmental drivers (e.g. Li et al. 2020).

4 POTENTIAL FUTURE L4_C PRODUCT UPDATES

Future releases of the SMAP L4_C operational product are expected to incorporate ongoing refinements and improvements in the SMAP brightness temperature observations and the GEOS land model assimilation system, as well as updates to other L4_C inputs. Future product releases may also incorporate additional refinements and improvements to the L4_C Terrestrial Carbon Flux (TCF) model. Significant product updates may include:

- *Improvements to the GEOS assimilation system.* The NASA GEOS system provides the daily surface meteorology and SMAP L4_SM surface and root soil moisture and soil temperature inputs required for L4_C production. The system undergoes periodic refinements and updates to the Catchment land surface model, assimilation framework, and observational inputs that may contribute to improvements in the L4_SM and L4_C products. These improvements will be accounted for in future product releases through L4_C recalibration and re-initialization procedures, and from more accurate L4_C model inputs.
- *Transition from MODIS to VIIRS as primary source for fPAR inputs.* L4_C operations require global operational fPAR time series as primary inputs to define vegetation photosynthetic canopy cover and phenology for estimating GPP. The current baseline for the fPAR inputs is the MODIS Terra 8-day 500m MOD15A2H (C6) record. However, the MODIS sensors on both NASA EOS Terra and Aqua satellites are nearing end-of-mission. The potential loss of MODIS fPAR inputs requires an alternative fPAR source to maintain optimal L4_C operations. A new capability was added to the L4_C v6 preprocessor allowing for the use of the JPSS/NPP VIIRS 8-day global 500m fPAR operational record (VNP15A2H) in lieu of the MOD15A2H baseline for L4_C production. The VNP15A2H fPAR is expected to become the new baseline for future L4_C operations and product releases following more extensive global testing.
- *Improvements to TCF model respiration phenology.* Planning is underway to evaluate potential improvements in model litterfall allocation and autotrophic respiration phenology gained from recent science advances (Endsley et al. 2022). More realistic representations of these factors could potentially improve the estimated seasonality in RECO and NEE, while enhancing product utility for some science applications (e.g. Byrne et al. 2020).

5 ACKNOWLEDGEMENTS

Funding for this work was provided by the SMAP mission. Computing resources were provided by the NASA Center for Climate Simulation. This work used eddy covariance data acquired by the FLUXNET community, which was supported by the CarboEuropeIP, CSIRO, FAO-GTOS-TCO, iLEAPS, Max Planck Institute for Biogeochemistry, National Science Foundation, National Research Infrastructure for Australia, Terrestrial Ecosystem Research Network, University of Tuscia, Université Laval and Environment Canada, US Department of Energy and NOAA ESRL, as well as many local funders including the Global Change Research Centre AS Czech Republic, Wisconsin Focus on Energy, and Forest Department of the Autonomous Province of Bolzano – CO_2-measuring station of Renon/Ritten. We thank Drs. A.E. Andrews, M. Aurela, D. Baldocchi, J. Beringer, P. Bolstad, J. Cleverly, B.D. Cook, K.J. Davis, A.R. Desai, D. Eamus, E. Euskirchen, J. Goodrich, L. Hutley, A. Kalhori, H. Kwon, B. Law, C. Macfarlane, W. Oechel, S. Prober, K. Rautiainen, R. Scott, H. Wheater, D. Zona and many other PIs for sharing their flux tower data.

6 REFERENCES

Baccini, A., S.J. Goetz, W.S. Walker, et al., 2012. Estimated carbon dioxide emissions from tropical deforestation improved by carbon-density maps. *Nature Climate Change*, **2**, 182-185.

Baker, D.F., R.M. Law, K.R. Gurney, et al. 2006. TransCom 3 inversion intercomparison: Impact of transport model errors on the interannual variability of regional CO2 fluxes, 1988-2003. *Global Geochemical Cycles* **20**(1), https://doi.org/10.1029/2004GB002439.

Baldocchi, D., 2008. Breathing of the terrestrial biosphere: lessons learned from a global network of carbon dioxide flux measurement systems. *Austr. J. Bot.*, **56**: 1-26.

Brodzik, M.J., B. Billingsley, T. Haran, B. Raup, and M.H. Savoie, 2012. EASE-Grid 2.0: Incremental but significant improvements for Earth-gridded data sets. *Int. J. Geo-Information* **1**(1), doi:10.3390-/ijgi1010032.

Byrne, B., J. Liu, M. Lee, et al., 2020. Improved constraints on northern extratropical CO_2 fluxes obtained by combining surface-based and space-based atmospheric CO_2 measurements. *JGR Atmospheres*, **125**(15), https://doi.org/10.1029/2019JD032029.

Colliander, A., R.H. Reichle, W.T. Crow, et al., 2022. Validation of soil moisture data products from the NASA SMAP mission. *JSTARS*, 15, https://doi.org/10.1109/JSTARS.2021.3124743.

Endsley, K.A., J.S. Kimball, R.H. Reichle, and J.D. Watts, 2020. Satellite monitoring of global surface soil organic carbon dynamics using the SMAP Level 4 Carbon product. *JGR Biogeosciences* **125**(12), e2020JG006100, https://doi.org/10.1029/2020JG006100.

Endsley, K.A., J.S. Kimball, R.H. Reichle. 2022. "Soil respiration phenology improves modeled phase of terrestrial net ecosystem exchange in northern hemisphere. *Journal of Advances in Modeling Earth Systems*. https://agupubs.onlinelibrary.wiley.com/doi/10.1029/2021MS002804

Entekhabi, D., E.G. Njoku, P.E. O'Neill, et al., 2010. The Soil Moisture Active and Passive (SMAP) Mission. *Proceedings of the IEEE* **98**(5), 704-716.

Entekhabi, D., S. Yueh, P. O'Neill, K. Kellogg et al., SMAP Handbook, JPL Publication, JPL 400-1567, Jet Propulsion Laboratory, Pasadena, California, 182 pages, 2014. https://smap.jpl.nasa.gov/files/smap2/SMAP_Handbook_FINAL_1_JULY_2014_Web.pdf.

Friedl, M.A., D. Sulla-Menashe, B. Tan, A. Schneider, N. Ramankutty, A. Sibley, and X. Huang, 2010. MODIS Collection 5 global land cover: Algorithm refinements and characterization of new datasets. *Remote Sensing of Environment* **114**(1), 168-182.

Gelaro, R., et al., 2017. The Modern-Era Retrospective Analysis for Research and Applications, Version-2 (MERRA-2), *Journal of Climate* **30**, 5419-5454, https://doi.org/10.1175/JCLI-D-16-0758.1.

Glassy, J., J.S. Kimball, R.H. Reichle, J.V. Ardizzone, G-K. Kim, R.A. Lucchesi, and B.H. Weiss, 2015. Soil Moisture Active Passive (SMAP) Mission Level 4 Carbon (L4_C) Product Specification Document. GMAO Office Note No. 12 (Version 1.9), 71 pp, NASA Goddard Space Flight Center, Greenbelt, MD, USA. Available from http://gmao.gsfc.nasa.gov/pubs/office_notes.

Hengl, T., J. M. de Jesus, G.B.M. Heuvelink, et al., 2017. SoilGrids250m: Global gridded soil information based on machine learning. *PLOS ONE*, **12**(2): https://doi.org/10.1371/journal.pone.0169748 .

Jackson, T., A. Colliander, J. Kimball, R. Reichle, W. Crow, D. Entekhabi, P. O'Neill, and E. Njoku, 2014. SMAP Science Data Calibration and Validation Plan. SMAP Project, JPL D-52544, Jet Propulsion Laboratory, Pasadena CA, 96 pp (http://smap.jpl.nasa.gov/files/smap2/CalVal_Plan_120706_pub.pdf).

Jones, L.A., J.S. Kimball, R.H. Reichle, N. Madani, J. Glassy, J.V. Ardizzone, A. Colliander, J. Cleverly, A.R. Desai, D. Eamus, E.S. Euskirchen, L. Hutley, C. Macfarlane, and R.L. Scott, 2017. The SMAP Level 4 Carbon product for monitoring ecosystem land-atmosphere CO2 exchange. *IEEE TGARS,* **55**(11), 6517-6532, doi: 10.1109/TGRS.2017.2729343.

Jung, M., C. Schwalm, M. Migliavacca, et al., 2020. Scaling carbon fluxes from eddy covariance sites to globe: synthesis and evaluation of the FLUXCOM approach. *Biogeosciences*, **17**, 1343-1365.

Kimball, J.S., L.A. Jones, J.P. Glassy, and R. Reichle, 2014. SMAP Algorithm Theoretical Basis Document, Release A: L4 Carbon Product. SMAP Project, JPL D-66484, Jet Propulsion Laboratory, Pasadena CA., 76 pp, (http://smap-archive.jpl.nasa.gov/files/smap2/L4_C_RevA.pdf).

Le Quéré, C., L. Barbero, J. Hauck, R. M. Andrew, J. G. Canadell, S. Sitch, and J. I. Korsbakken, 2018. Global Carbon Budget 2018. *Earth System Science Data* **10**, 2141–2194.

Li, X., J. Xiao, B. He, et al. 2018. Solar-induced chlorophyll fluorescence is strongly correlated with terrestrial photosynthesis for a wide variety of biomes: First global analysis based on OCO-2 and flux tower observations. *Global Change Biology* **24**(9), 3990-4008.

Li, X., J. Xiao, J.S. Kimball, R.H. Reichle, R.L. Scott, M.E. Litvak, G. Bohrer, and C. Frankenberg, 2020. Synergistic use of SMAP and OCO-2 data in assessing the responses of ecosystem productivity to the 2018 U.S. drought. *Remote Sensing of Environment*, **251**, 112062, https://doi.org/10.1016/j.rse.2020.112062.

Liu, Z., J.S. Kimball, N. Parazoo, A. Ballantyne, W. Wen, R. Reichle, C. Pan, J. Watts, O. Sonnentag, P. Marsh, M. Hurkuck, M. Helbig, W. Quinton, D. Zona, M. Ueyama, H. Kobayashi, and E. Euskirchen, 2019. Increased high-latitude photosynthetic carbon gain offset by respiration carbon loss during an anomalous warm winter to spring transition. *Global Change Biology*, **26**(2), 682-696, DOI:10.1111/gcb.14863.

Madani, N., J.S. Kimball, and S.W. Running, 2017. Improving global gross primary productivity estimates by computing optimal light use efficiencies using flux tower data. *J. Geophys. Res. Biogeosci*., **122**(11), 2939-2951.

Madani, N., J.S. Kimball, L.A. Jones, N.C. Parazoo, and K. Guan, 2017. Global analysis of bioclimatic controls on ecosystem productivity using satellite observations of solar-induced chlorophyll fluorescence. *Remote Sensing*, **9**, 530.

Myneni, R., Y. Knyazikhin, T. Park. MOD15A2H MODIS/Terra Leaf Area Index/FPAR 8-Day L4 Global 500m SIN Grid V006. 2015, distributed by NASA EOSDIS Land Processes DAAC, https://doi.org/10.5067/MODIS/MOD15A2H.006. Accessed 2022-02-13.

Pastorello, G., C. Trotta, E. Canfora, H. Chu, D. Christianson, Y.-W. Cheah, C. Poindexter, J. Chen, A. Elbashandy, M. Humphrey, P. Isaac, D. Polidori, A. Ribeca, C. van Ingen, L. Zhang, B. Amiro, C. Ammann, M. A. Arain, J. Ardö, T. Arkebauer, et al. 2020. The FLUXNET2015 dataset and the ONEFlux processing pipeline for eddy covariance data. *Scientific Data* 7 (1):225.

Porcar-Castell, A., E. Tyystjarvi, J. Atherton, et al., 2014. Linking chlorophyll a fluorescence to photosynthesis for remote sensing applications: mechanisms and challenges. *Journal of Experimental Botany*, **66**(19), doi:101093/jxb/eru191.

Reichle, R.H., Q. Liu, J.V. Ardizzone, W.T. Crow, G.J.M. De Lannoy, J. Dong, J.S. Kimball, and R.D. Koster, 2020. The contributions of gauge-based precipitation and SMAP brightness temperature observations to the skill of the SMAP Level-4 Soil Moisture product. *J. Hydrometeorology*, **22**(2), DOI:10.1175/JHM-D-20-0217.1.

Reichle, R., Q. Liu, R.D. Koster, J.V. Ardizzone, A. Colliander, W.T. Crow, G. De Lannoy, J.S. Kimball, J. Kolassa, and S.P. Mahanama, 2019. Version 4 of the SMAP Level-4 soil moisture algorithm and data product. *Journal of Advances in Modeling Earth Systems*, **11**(10), doi:10.1029/2019MS001729.

Reichle, R.H., Q. Liu, R.D. Koster, J. Ardizzone, A. Colliander, W. Crow, G.J.M. De Lannoy, and J.S. Kimball, 2022. Soil Moisture Active Passive (SMAP) Project Assessment Report for Version 6 of the L4_SM Data Product. Technical Report Series on Global Modeling and Data Assimilation, NASA/TM-2022-104606, Volume 60, 68pp.

Schimel, D., R. Pavlick, J.B. Fisher, G.P. Asner, S. Saatchi, P. Townsend, C. Miller, C. Frankenberg, K. Hibbard, and P. Cox, 2015. Observing terrestrial ecosystems and the carbon cycle from space. *Global Change Biology* **21**(5), 1762-1776.

Tarnocai, C., J. G. Canadell, E. A. G. Schuur, P. Kuhry, G. Mazhitova, and S. Zimov. 2009. Soil organic carbon pools in the northern circumpolar permafrost region. *Global Biogeochemical Cycles* **23** (2).

Ukkola, A., G. Abramowitz, and M. De Kauwe. 2021. A flux tower dataset tailored for land model evaluation. *Earth System Science Data Discussions*. DOI: 10.5194/essd-2021-181

Wurster, P.M., M. Maneta, J.S. Kimball, K.A. Endsley, and S. Begueria, 2020. Monitoring crop status in the continental United States using the SMAP Level 4 Carbon product. *Frontiers in Big Data*, **3**, 597720.

Xu, B., T. Park, K. Yan, C. Chen, Y. Zeng, W. Song, G. Yin, J. Li, Q. Liu, Y. Knyazikhin, and R. B. Myneni. 2018. Analysis of global LAI/FPAR products from VIIRS and MODIS sensors for spatio-temporal consistency and uncertainty from 2012-2016. *Forests* **9** (2), 1–21.

Yan, K., J. Pu, T. Park, B. Xu, Y. Zeng, G. Yan, M. Weiss, Y. Knyazikhin, and R. B. Myneni. 2021. Performance stability of the MODIS and VIIRS LAI algorithms inferred from analysis of long time series of products. *Remote Sensing of Environment* **260**, 112438.

Yi, Y., J.S. Kimball, L.A. Jones, R.H. Reichle, R. Nemani, and H.A. Margolis, 2013. Recent climate and fire disturbance impacts on boreal and arctic ecosystem productivity estimated using a satellite-based terrestrial carbon flux model. *J. Geophys. Res*. *Biogeosci*., **118**, 1-17.

Zhang, Y., J. Joiner, S. Hamed Alemohammad, S. Zhou, and P. Gentine. 2018. A global spatially contiguous solar-induced fluorescence (CSIF) dataset using neural networks. *Biogeosciences* **15** (19), 5779–5800.

Previous Volumes in This Series

Volume 1 September 1994	*Documentation of the Goddard Earth Observing System (GEOS) general circulation model - Version 1* L.L. Takacs, A. Molod, and T. Wang
Volume 2 October 1994	*Direct solution of the implicit formulation of fourth order horizontal diffusion for gridpoint models on the sphere* Y. Li, S. Moorthi, and J.R. Bates
Volume 3 December 1994	*An efficient thermal infrared radiation parameterization for use in general circulation models* M.-D. Chou and M.J. Suarez
Volume 4 January 1995	*Documentation of the Goddard Earth Observing System (GEOS) Data Assimilation System - Version 1* James Pfaendtner, Stephen Bloom, David Lamich, Michael Seablom, Meta Sienkiewicz, James Stobie, and Arlindo da Silva
Volume 5 April 1995	*Documentation of the Aries-GEOS dynamical core: Version 2* Max J. Suarez and Lawrence L. Takacs
Volume 6 April 1995	*A Multiyear Assimilation with the GEOS-1 System: Overview and Results* Siegfried Schubert, Chung-Kyu Park, Chung-Yu Wu, Wayne Higgins, Yelena Kondratyeva, Andrea Molod, Lawrence Takacs, Michael Seablom, and Richard Rood
Volume 7 September 1995	*Proceedings of the Workshop on the GEOS-1 Five-Year Assimilation* Siegfried D. Schubert and Richard B. Rood
Volume 8 March 1996	*Documentation of the Tangent Linear Model and Its Adjoint of the Adiabatic Version of the NASA GEOS-1 C-Grid GCM: Version 5.2* Weiyu Yang and I. Michael Navon
Volume 9	*Energy and Water Balance Calculations in the Mosaic LSM*

March 1996 — Randal D. Koster and Max J. Suarez

Volume 10 — *Dynamical Aspects of Climate Simulations Using the GEOS General Circulation Model*
April 1996 — Lawrence L. Takacs and Max J. Suarez

Volume 11 — *Documentation of the Tangent Linear and Adjoint Models of the Relaxed Arakawa-Schubert Moisture Parameterization Package of the NASA GEOS-1 GCM (Version 5.2)*
May 1997 — Weiyu Yang, I. Michael Navon, and Ricardo Todling

Volume 12 — *Comparison of Satellite Global Rainfall Algorithms*
August 1997 — Alfred T.C. Chang and Long S. Chiu

Volume 13 — *Interannual Variability and Potential Predictability in Reanalysis Products*
December 1997 — Wie Ming and Siegfried D. Schubert

Volume 14 — *A Comparison of GEOS Assimilated Data with FIFE Observations*
August 1998 — Michael G. Bosilovich and Siegfried D. Schubert

Volume 15 — *A Solar Radiation Parameterization for Atmospheric Studies*
June 1999 — Ming-Dah Chou and Max J. Suarez

Volume 16 — *Filtering Techniques on a Stretched Grid General Circulation Model*
November 1999 — Lawrence Takacs, William Sawyer, Max J. Suarez, and Michael S. Fox-Rabinowitz

Volume 17 — *Atlas of Seasonal Means Simulated by the NSIPP-1 Atmospheric GCM*
July 2000 — Julio T. Bacmeister, Philip J. Pegion, Siegfried D. Schubert, and Max J. Suarez

Volume 18 — *An Assessment of the Predictability of Northern Winter Seasonal Means with the NSIPP1 AGCM*
December 2000 — Philip J. Pegion, Siegfried D. Schubert, and Max J. Suarez

Volume 19 — *A Thermal Infrared Radiation Parameterization for Atmospheric Studies*

July 2001 — Ming-Dah Chou, Max J. Suarez, Xin-Zhong Liang, and Michael M.-H. Yan

Volume 20 — *The Climate of the FVCCM-3 Model*

August 2001 — Yehui Chang, Siegfried D. Schubert, Shian-Jiann Lin, Sharon Nebuda, and Bo-Wen Shen

Volume 21 — *Design and Implementation of a Parallel Multivariate Ensemble Kalman Filter for the Poseidon Ocean General Circulation Model*

September 2001 — Christian L. Keppenne and Michele M. Rienecker

Volume 22 — *A Coupled Ocean-Atmosphere Radiative Model for Global Ocean Biogeochemical Models*

August 2002 — Watson W. Gregg

Volume 23 — *Prospects for Improved Forecasts of Weather and Short-term Climate Variability on Subseasonal (2-Week to 2-Month) Time Scales*

November 2002 — Siegfried D. Schubert, Randall Dole, Huang van den Dool, Max J. Suarez, and Duane Waliser

Volume 24 — *Temperature Data Assimilation with Salinity Corrections: Validation for the NSIPP Ocean Data Assimilation System in the Tropical Pacific Ocean, 1993–1998*

July 2003 — Alberto Troccoli, Michele M. Rienecker, Christian L. Keppenne, and Gregory C. Johnson

Volume 25 — *Modeling, Simulation, and Forecasting of Subseasonal Variability*

December 2003 — Duane Waliser, Siegfried D. Schubert, Arun Kumar, Klaus Weickmann, and Randall Dole

Volume 26 — *Documentation and Validation of the Goddard Earth Observing System (GEOS) Data Assimilation System – Version 4*

April 2005 — Senior Authors: S. Bloom, A. da Silva and D. Dee

Contributing Authors: M. Bosilovich, J-D. Chern, S. Pawson, S. Schubert, M. Sienkiewicz, I. Stajner, W-W. Tan, and M-L. Wu

Volume 27

December 2008

The GEOS-5 Data Assimilation System - Documentation of Versions 5.0.1, 5.1.0, and 5.2.0.

M.M. Rienecker, M.J. Suarez, R. Todling, J. Bacmeister, L. Takacs, H.-C. Liu, W. Gu, M. Sienkiewicz, R.D. Koster, R. Gelaro, I. Stajner, and J.E. Nielsen

Volume 28

April 2012

The GEOS-5 Atmospheric General Circulation Model: Mean Climate and Development from MERRA to Fortuna

Andrea Molod, Lawrence Takacs, Max Suarez, Julio Bacmeister, In-Sun Song, and Andrew Eichmann

Volume 29

June 2012

Atmospheric Reanalyses – Recent Progress and Prospects for the Future.

A Report from a Technical Workshop, April 2010

Michele M. Rienecker, Dick Dee, Jack Woollen, Gilbert P. Compo, Kazutoshi Onogi, Ron Gelaro, Michael G. Bosilovich, Arlindo da Silva, Steven Pawson, Siegfried Schubert, Max Suarez, Dale Barker, Hirotaka Kamahori, Robert Kistler, and Suranjana Saha

Volume 30

December 2012

The GEOS-iODAS: Description and Evaluation

Guillaume Vernieres, Michele M. Rienecker, Robin Kovach and Christian L. Keppenne

Volume 31

March 2013

Global Surface Ocean Carbon Estimates in a Model Forced by MERRA

Watson W. Gregg, Nancy W. Casey and Cécile S. Rousseaux

Volume 32

March 2014

Estimates of AOD Trends (2002-2012) over the World's Major Cities based on the MERRA Aerosol Reanalysis

Simon Provencal, Pavel Kishcha, Emily Elhacham, Arlindo M. da Silva, and Pinhas Alpert

Volume 33

August 2014

The Effects of Chlorophyll Assimilation on Carbon Fluxes in a Global Biogeochemical Model

Cécile S. Rousseaux and Watson W. Gregg

Volume 34
September 2014

Background Error Covariance Estimation using Information from a Single Model Trajectory with Application to Ocean Data Assimilation into the GEOS-5 Coupled Model

Christian L. Keppenne, Michele M. Rienecker, Robin M. Kovach, and Guillaume Vernieres

Volume 35
December 2014

Observation-Corrected Precipitation Estimates in GEOS-5

Rolf H. Reichle and Qing Liu

Volume 36
March 2015

Evaluation of the 7-km GEOS-5 Nature Run

Ronald Gelaro, William M. Putman, Steven Pawson, Clara Draper, Andrea Molod, Peter M. Norris, Lesley Ott, Nikki Prive, Oreste Reale, Deepthi Achuthavarier, Michael Bosilovich, Virginie Buchard, Winston Chao, Lawrence Coy, Richard Cullather, Arlindo da Silva, Anton Darmenov, Ronald M. Errico, Marangelly Fuentes, Min-Jeong Kim, Randal Koster, Will McCarty, Jyothi Nattala, Gary Partyka, Siegfried Schubert, Guillaume Vernieres, Yuri Vikhliaev, and Krzysztof Wargan

Volume 37
March 2015

Maintaining Atmospheric Mass and Water Balance within Reanalysis

Lawrence L. Takacs, Max Suarez, and Ricardo Todling

Volume 38
September 2015

The Quick Fire Emissions Dataset (QFED) – Documentation of versions 2.1, 2.2 and 2.4

Anton S. Darmenov and Arlindo da Silva

Volume 39
September 2015

Land Boundary Conditions for the Goddard Earth Observing System Model Version 5 (GEOS-5) Climate Modeling System - Recent Updates and Data File Descriptions

Sarith Mahanama, Randal Koster, Gregory Walker, Lawrence Takacs, Rolf Reichle, Gabrielle De Lannoy, Qing Liu, Bin Zhao, and Max Suarez

Volume 40
October 2015

Soil Moisture Active Passive (SMAP) Project Assessment Report for the Beta-Release L4_SM Data Product

Rolf H. Reichle, Gabrielle J. M. De Lannoy, Qing Liu, Andreas Colliander, Austin Conaty, Thomas Jackson, John Kimball, and Randal D. Koster

Volume 41 *GDIS Workshop Report*

October 2015 Siegfried Schubert, Will Pozzi, Kingtse Mo, Eric Wood, Kerstin Stahl, Mike Hayes, Juergen Vogt, Sonia Seneviratne, Ron Stewart, Roger Pulwarty, and Robert Stefanski

Volume 42 *Soil Moisture Active Passive (SMAP) Project Calibration and Validation for the L4_C Beta-Release Data Product*

November 2015 John Kimball, Lucas Jones, Joseph Glassy, E. Natasha Stavros, Nima Madani, Rolf Reichle, Thomas Jackson, and Andreas Colliander

Volume 43 *MERRA-2: Initial Evaluation of the Climate*

September 2015 Michael G. Bosilovich, Santha Akella, Lawrence Coy, Richard Cullather, Clara Draper, Ronald Gelaro, Robin Kovach, Qing Liu, Andrea Molod, Peter Norris, Krzysztof Wargan, Winston Chao, Rolf Reichle, Lawrence Takacs, Yury Vikhliaev, Steve Bloom, Allison Collow, Stacey Firth, Gordon Labow, Gary Partyka, Steven Pawson, Oreste Reale, Siegfried Schubert, and Max Suarez

Volume 44 *Estimation of the Ocean Skin Temperature using the NASA GEOS Atmospheric Data Assimilation System*

February 2016 Santha Akella, Ricardo Todling, Max Suarez

Volume 45 *The MERRA-2 Aerosol Assimilation*

October 2016 C. A. Randles, A. M. da Silva, V. Buchard, A. Darmenov, P. R. Colarco, V. Aquila, H. Bian, E. P. Nowottnick, X. Pan, A. Smirnov, H. Yu, and R. Govindaraju

Volume 46 *The MERRA-2 Input Observations: Summary and Assessment*

October 2016 Will McCarty, Lawrence Coy, Ronald Gelaro, Albert Huang, Dagmar Merkova, Edmond B. Smith, Meta Sienkiewicz, and Krzysztof Wargan

Volume 47 *An Evaluation of Teleconnections Over the United States in an Ensemble of AMIP Simulations with the MERRA-2 Configuration of the GEOS Atmospheric Model.*

May 2017 Allison B. Marquardt Collow, Sarith P. Mahanama, Michael G. Bosilovich, Randal D. Koster, and Siegfried D. Schubert

Volume 48

July 2017

Description of the GMAO OSSE for Weather Analysis Software Package: Version 3

Ronald M. Errico, Nikki C. Prive, David Carvalho, Meta Sienkiewicz, Amal El Akkraoui, Jing Guo, Ricardo Todling, Will McCarty, William M. Putman, Arlindo da Silva, Ronald Gelaro, and Isaac Moradi

Volume 49

March 2018

Preliminary Evaluation of Influence of Aerosols on the Simulation of Brightness Temperature in the NASA Goddard Earth Observing System Atmospheric Data Assimilation System

Jong Kim, Santha Akella, Will McCarty, Ricardo Todling, and Arlindo M. da Silva

Volume 50

March 2018

The GMAO Hybrid Ensemble-Variational Atmospheric Data Assimilation System: Version 2.0

Ricardo Todling and Amal El Akkraoui

Volume 51

July 2018

The Atmosphere-Ocean Interface Layer of the NASA Goddard Earth Observing System Model and Data Assimilation System

Santha Akella and Max Suarez

Volume 52

July 2018

Soil Moisture Active Passive (SMAP) Project Assessment Report for Version 4 of the L4_SM Data Product

Rolf H. Reichle, Qing Liu, Randal D. Koster, Joe Ardizzone, Andreas Colliander, Wade Crow, Gabrielle J. M. De Lannoy, and John Kimball

Volume 53

October 2019

Ensemble Generation Strategies Employed in the GMAO GEOS-S2S Forecast System

Siegfried Schubert, Anna Borovikov, Young-Kwon Lim, and Andrea Molod

Volume 54

August 2020

Position Estimation of Atmospheric Motion Vectors for Observation System Simulation Experiments

David Carvalho and Will McCarty

Volume 55 February 2021	*A Phenomenon-Based Decomposition of Model-Based Estimates of Boreal Winter ENSO Variability* Schubert, Siegfried, Young-Kwon Lim, Andrea Molod, and Alllison Collow
Volume 56 June 2021	*Validation Assessment for the Soil Moisture Active Passive (SMAP) Level 4 Carbon (L4_C) Data Product Version 5* John S. Kimball, K. Arthur Endsley, Tobias Kundig, Joseph Glassy, Rolf H. Reichle, and Joseph V. Ardizzone
Volume 57 July 2021	*Tendency Bias Correction in the GEOS AGCM* Yehui Chang, Siegfried Schubert, Randal Koster, and Andrea Molod
Volume 58 August 2021	*Soil Moisture Active Passive (SMAP) Project Assessment Report for Version 5 of the L4_SM Data Product* Rolf H. Reichle, Qing Liu, Randal D. Koster, Joseph V. Ardizzone, Andreas Colliander, Wade Crow, Gabrielle J. M. De Lannoy, and John S. Kimball
Volume 59 November 2021	*Observation-Corrected Land Surface Precipitation for the SMAP Level 4 Soil Moisture (Version 6) Product and the GEOS R21C Reanalysis* Rolf H. Reichle and Qing Liu
Volume 60 January 2022	*Soil Moisture Active Passive (SMAP) Project Assessment Report for Version 6 of the L4_SM Data Product* Rolf H. Reichle, Qing Liu, Randal D. Koster, Joseph V. Ardizzone, Andreas Colliander, Wade Crow, Gabrielle J. M. De Lannoy, and John S. Kimball